Chemical Geology 480 (2018) 44–57

Contents lists available at ScienceDirect

Chemical Geology

journal homepage: www.elsevier.com/locate/chemgeo

Spatially heterogeneous argon-isotope systematics and apparent $^{40}Ar/^{39}Ar$ ages in perlitised obsidian

Stephanie Flude[a,*], Hugh Tuffen[b], Sarah C. Sherlock[c]

[a] School of Earth, Environment and Ecosystems, The Open University, Walton Hall, Milton Keynes MK7 6AA, United Kingdom
[b] Lancaster Environment Centre, Lancaster University, Lancaster LA1 4YQ, United Kingdom
[c] School of Physical Sciences, The Open University, Walton Hall, Milton Keynes MK7 6AA, United Kingdom

ARTICLE INFO

Keywords:
$^{40}Ar/^{39}Ar$-dating
Obsidian
Diffusion
Ar-isotopes

ABSTRACT

In situ laser ablation Ar-isotope analyses of variably hydrated and devitrified obsidian from the ~27 Ma Cochetopa Dome, San Juan, USA, reveal complex interplay between degassing of initial Ar and absorption of atmospheric Ar. These processes have locally modified the Ar-isotope composition of the obsidian and led to spurious, spatially-heterogeneous Ar-isotope and $^{40}Ar/^{39}Ar$ age data. Small perlite beads exhibit older apparent Ar-ages at the rims than the cores. This is interpreted as an apparent excess of ^{40}Ar at the rims, produced either by a) diffusion of excess ^{40}Ar into the bead during flushing of the lava with excess ^{40}Ar-bearing volcanic gas, or by b) isotopic fractionation during degassing of initial Ar, causing preferential loss of ^{36}Ar over ^{40}Ar at the bead rims. The second interpretation is favoured by a relative enrichment of ^{36}Ar in the core of a perlite bead along a microlite-free (poorly degassed) flow band, and by a lack of age variation in a larger, fresh, well-degassed perlite bead. These isotopic gradients were later overprinted during glass hydration by absorption of Ar with near-atmospheric composition, resulting in elevated ^{36}Ar and reduced radiogenic $^{40}Ar^*$ yields at the rims of perlite beads.

These complex interactions essentially represent the mixing of three distinct Ar reservoirs: initial trapped Ar that may or may not be fractionated, an isotopically atmospheric Ar component introduced during hydration, and radiogenic $^{40}Ar^*$. Such reservoir mixing is the underlying reason for poor correlations on isotope correlation diagrams and the difficulties in validating the composition of the non-radiogenic Ar component. We thus suggest that high ^{36}Ar yields are a combination of the incomplete degassing of initial (possibly magmatic) Ar and the gain of Ar during interaction between the obsidian and meteoric/atmospheric fluids. Our analyses emphasise the challenging nature of $^{40}Ar/^{39}Ar$ dating obsidian samples, but also point to possible solutions by careful sample characterisation and selection of highly degassed samples.

1. Introduction

Relative and absolute chronological data is of utmost importance in interpreting the products of volcanic eruptions and how they affected the local, regional and wider environment. As isotope-dating techniques improve, so does the precision on radiometric ages, allowing precise correlations between volcanic eruptions and climate change events to be extended to prehistoric eruptions and those not represented in ice cores (c.f. Clausen et al., 1997; Gao et al., 2008; Sigl et al., 2015). Such correlations are particularly important because they facilitate a deeper understanding of both the potential environmental impact of volcanic eruptions, and the timescales of past climate change, as well as postulated feedbacks between volcanism and climate (e.g. Huybers and Langmuir, 2009; Rampino and Self, 1992). Precise dating of large volcanic eruptions that can be recognised in Arctic and/or Antarctic ice cores such as the Younger Toba Tuff (Mark et al., 2014; Storey et al., 2012) allows calibration of Quaternary climate records. However, the products of smaller volcanic eruptions can be useful in interpreting localised environmental conditions, especially at volcanic systems with temporally-variable snow and ice cover, such as in Chile (Lachowycz et al., 2015; Mee et al., 2009, 2006), Iceland (McGarvie et al., 2007; Stevenson et al., 2009, 2006; Tuffen et al., 2010) and Antarctica (Smellie et al., 2014, 2011a, 2011b). Precise dates for this type of volcanic deposit could provide a wealth of data on the timing and timescales of local environmental changes, such as ice sheet growth and retreat, which reflect broader climatic events (McGarvie, 2009). A number of recent studies highlight the potential benefits of this combination of age and volcanic/environmental facies data (Flude

* Corresponding author at: Edinburgh, United Kingdom.
E-mail address: sflude@gmail.com (S. Flude).

http://dx.doi.org/10.1016/j.chemgeo.2017.05.018
Received 30 November 2016; Received in revised form 16 May 2017; Accepted 17 May 2017
Available online 19 May 2017

et al., 2010, 2008; McGarvie et al., 2007; Mee et al., 2009) but were unable to unlock the full potential of the technique due to difficulties in achieving the required precision. For instance, meaningful comparisons of environmental events with the benthic oxygen isotope curve, used as a proxy for global temperature, require the age errors to be a maximum of 2–3 thousand years, a level of precision rarely achieved to date. Typical 1 σ $^{40}Ar/^{39}Ar$ dating errors on young glaciovolcanics are 5–23 ka (Flude et al., 2010), 6–20 ka (McGarvie et al., 2006), 5–66 ka (Guillou et al., 2010) and 24 ka, (McGarvie et al., 2007). Young, high-precision radiometric ages, such as the ages for the Younger Toba Tuff (73.88 ± 0.32 ka - (Storey et al., 2012); 75.0 ± 0.9 ka - (Mark et al., 2014) require high-K, isotopically-simple samples. In the case of $^{40}Ar/^{39}Ar$ dating, a retentive, K-rich mineral phase such as sanidine, which experienced a simple cooling history, is ideal. Unfortunately, such phases may not be present in volcanic deposits of interest. For example, Iceland hosts many volcanic deposits that can provide copious data on past ice sheet thickness and landscape change (Helgason and Duncan, 2013; McGarvie, 2009; Owen et al., 2012; Stevenson et al., 2006), but most Icelandic magmas are of tholeiitic or transitional-alkaline lineage (Jónasson, 1994), making K-bearing phenocrysts notably scarce.

Obsidian, silicic volcanic glass, is however, relatively common, often containing several percent K_2O (Flude et al., 2010, 2008; Jónasson, 1994; McGarvie, 1984; McGarvie et al., 2007; Owen et al., 2012), and most recent attempts at dating Icelandic volcanics have employed $^{40}Ar/^{39}Ar$ dating of obsidian, albeit with varying degrees of success. Other recent studies have shown that $^{40}Ar/^{39}Ar$ dating of obsidian could be applied to a wide range of localities and research problems (Lipman and McIntosh, 2008; Morgan et al., 2009). However, first standardisation and optimisation of $^{40}Ar/^{39}Ar$ dating techniques as applied to obsidian is necessary, requiring understanding of the processes affecting obsidian during and after cooling.

Obsidian is a volcanic glass that forms by rapid cooling of silica rich melt. It may form by chilling of lava in contact with air, water or ice, as highly welded facies in pyroclastic deposits, and as chilled margins of shallow silicic intrusions. Devitrification of obsidian can occur over a wide temperature range. Above and around T_g, at temperatures of 800–600 °C, spherulite and globulite growth converts obsidian to anhydrous masses of sanidine, cristobalite and Fe-Ti oxides (Castro et al., 2008; Gardner et al., 2012; Watkins et al., 2008), a process thought to continue to rather lower temperatures (300 °C; Befus, 2016). At temperatures below 400 °C devitrification is thought to be largely ineffective, but can be facilitated by the presence of alkali-rich hydrothermal fluids, which can promote rapid devitrification (in a matter of days) at ≪300 °C (Lofgren, 1971). Devitrification of obsidian promotes redistribution of volatiles.

Perlitisation involves the ingress of external water into obsidian via the formation of curving fractures, which intersect to create beads of non-hydrated glass surrounded by zones of strong H_2O enrichment along concentric fractures (e.g. Denton et al., 2012, 2009; Friedman et al., 1966; Jezek and Noble, 1978; von Aulock et al., 2013). Initial fracturing is attributed to cooling contraction (Denton et al., 2012), and followed by a stress corrosion process, in which addition of H_2O to crack tips triggers a volume change in the glass that drives further crack advance. Perlitisation is thought to occur at elevated temperatures – between the glass transition (T_g ~600–700 °C) to ~300–400 °C (Denton et al., 2012; von Aulock et al., 2013), but can continue at ambient temperature, albeit with drastically lower rates of diffusive hydration. Perlitisation can induce ion exchange, with local enrichment in K_2O and depletion in Na_2O corresponding with zones of hydration along perlitic fractures (Jezek and Noble, 1978).

Significant difficulties in achieving accurate and precise K-Ar and $^{40}Ar/^{39}Ar$ ages on obsidian have been encountered (Flude et al., 2010; Kaneoka, 1972; Morgan et al., 2009; Vogel et al., 2006). In this paper we summarise the current understanding of the difficulties in dating obsidian using the $^{40}Ar/^{39}Ar$ method, and begin to investigate ways in which the technique might be improved through more complete understanding of $^{40}Ar/^{39}Ar$ systematics in obsidian, including refined sample characterisation and selection. We have used variably hydrated and devitrified obsidian from the San Juan volcanic field, Colorado, USA, and performed in-situ Ar-isotope analyses and infra-red spectroscopic analyses to measure the distribution of Ar-isotopes and water concentrations in the various obsidian microtextures.

1.1. $^{40}Ar/^{39}Ar$ dating of obsidian – the problems

K-Ar and $^{40}Ar/^{39}Ar$ dating often rely on the assumption that Ar-isotopes within a sample are the product of mixing between two end-member reservoirs: radiogenic $^{40}Ar^*$, derived from radioactive decay of ^{40}K, and a single trapped component, representing the argon content of the sample at the time it cooled through the closure temperature for argon. A basic age determination assumes that the trapped component is atmospheric ($^{40}Ar/^{36}Ar$ = 298.5 - Lee et al., 2006) and uses the abundance of ^{36}Ar to correct the measured ^{40}Ar value for trapped air. The Ar-isotope composition of the trapped component can be characterised by carrying out multiple measurements on the same sample and plotting the results on an isotope correlation diagram (isochron). Many studies of $^{40}Ar/^{39}Ar$ dating on a range of materials find that the trapped component is indeed atmospheric (McDougall and Harrison, 1999). Trapped Ar isotopes with $^{40}Ar/^{36}Ar > 298.5$ are, however, common, indicating the presence of excess ^{40}Ar in the sample (Kelley, 2002). In these cases, plotting of an isochron can determine the true $^{40}Ar/^{39}Ar$ age and characterise the isotopic composition of the trapped argon, but only when the system represents mixing between radiogenic argon and a single reservoir or trapped, excess ^{40}Ar-bearing argon.

Observed difficulties in K-Ar and $^{40}Ar/^{39}Ar$ dating obsidian can be generally classified as one of four problems:

1. Post-cooling hydration may mobilise alkali metals and release Ar, resulting in loss of $^{40}Ar^*$ and/or K (Cerling et al., 1985; Kaneoka, 1972, 1969). Water-derived H^+ substitutes for Na^+ or K^+, facilitating charge balance and allowing the alkalis to migrate out of the glass structure (Cerling et al., 1985), while alteration of the glass structure promotes loss of argon. Loss of $^{40}Ar^*$ results in spuriously young apparent Ar-ages, while loss of K results in spuriously old apparent Ar-ages.
2. Many studies have noted high proportions of ^{36}Ar, presumed to be a trapped atmospheric component. This large, trapped atmospheric argon component dilutes the $^{40}Ar^*$ signal and reduces age precision. Although atmospheric Ar entrapment occurs in other volcanic minerals, including micas, these are rarely noted in the literature and it appears particularly problematic for obsidians (Flude et al., 2010; Morgan et al., 2009; Vogel et al., 2006). High atmospheric Ar abundances may result from incomplete degassing of the melt during eruption (assuming an initial trapped argon component that is isotopically atmospheric), the incorporation of meteoric fluid into the obsidian during eruption, cooling and/or hydration, and via microcrack generation during sampling and sample preparation (Ballentine and Barfod, 2000). Distinguishing these trapped argon sources has thus far received little scientific attention and models for identifying these different components do not currently exist.
3. Non-radiogenic and non-atmospheric ^{40}Ar (excess ^{40}Ar) may be present in obsidian samples (Flude et al., 2010), a common problem for all fields of $^{40}Ar/^{39}Ar$ dating (Kelley, 2002). Failure to identify and account for excess ^{40}Ar leads to spuriously old apparent ages. It is thought to originate from equilibration in an environment with a greater than atmospheric $^{40}Ar/^{36}Ar$ ratio, and so may be particularly problematic for primitive melts with a large proportion of mantle volatiles, and for volcanic systems set in old continental crust where $^{40}Ar^*$ from old, K-rich host rocks becomes assimilated into magma as excess ^{40}Ar. Excess ^{40}Ar is identified by plotting multiple analyses (either stepped heating or single grain fusions) on an isotope

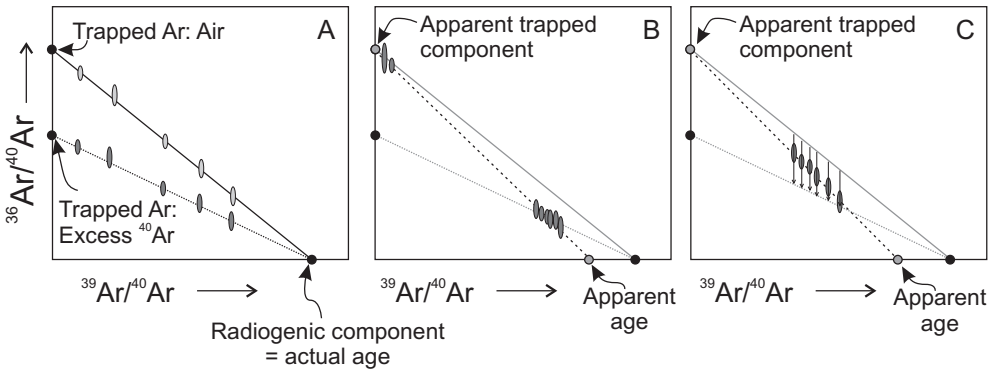

Fig. 1. Schematic isochron diagrams showing how uneven distribution of excess ^{40}Ar, or mixing of more than two argon reservoirs can produce statistically valid but meaningless isochrons (based on Kuiper, 2002) A: Two hypothetical data sets showing mixing between a radiogenic and trapped air component (light grey symbols, solid line) and a radiogenic and trapped component with excess ^{40}Ar (dark grey symbols, dotted line). B: Hypothetical data of an excess ^{40}Ar bearing sample that produces data with little scatter (data lie on the excess ^{40}Ar isochron) and that also contains an atmospheric trapped component. The isochron produced by such data (dashed line) would produce an atmospheric intercept and an apparent age that is too old. C: Hypothetical data for an excess ^{40}Ar bearing sample where the excess ^{40}Ar is unevenly distribute throughout the sample. Small arrows show how the Ar-isotope composition shifts from the radiogenic-air mixing line to the radiogenic-excess ^{40}Ar mixing line with variable addition of excess ^{40}Ar. Such data may form a correlation giving radiogenic and trapped compositions that are meaningless, with apparent ages that are either too old or too young.

correlation diagram (isochron) where the intercept on the y-axis represents the composition of the non-radiogenic, i.e. trapped, Ar. In simple systems the intercept will have an atmospheric value ($^{40}Ar/^{36}Ar = 295.5$) if there is no excess ^{40}Ar, or, if excess ^{40}Ar is present, $^{40}Ar/^{36}Ar$ will be > 295.5. However, samples containing excess ^{40}Ar may produce isochrons with an atmospheric intercept if either the excess ^{40}Ar is unevenly distributed through the sample (Sherlock and Arnaud, 1999), or if the sample also contains a large proportion of atmospheric Ar – i.e. three-component mixing between radiogenic $^{40}Ar^*$, trapped gas with excess ^{40}Ar and atmospheric Ar (Kuiper, 2002) (Fig. 1). In addition, the spread in $^{40}Ar/^{39}Ar$ values from obsidian stepped heating data may be insufficient to produce an isochron (Morgan et al., 2009), preventing the fingerprinting of the non-radiogenic Ar component (Fig. 1).

4. Some studies have identified obsidian samples containing trapped argon with $^{40}Ar/^{36}Ar < 295.5$ – i.e. they contain an apparent excess of ^{36}Ar (Morgan et al., 2009; Vogel et al., 2006). If not accounted for, this will lead to spuriously young apparent ages due to over-correction of atmospheric ^{40}Ar. Morgan et al. (2009) attributed low $^{40}Ar/^{36}Ar$ ratios to kinetic mass fractionation of Ar-isotopes during incomplete equilibration of the obsidian with the atmosphere during quenching. Similarly, Brown et al. (2009) suggested a two-stage isotope fractionation mechanism, with atmospheric argon initially being fractionated via Soret diffusion within a gaseous environment experiencing a strong temperature gradient (e.g. air in a crack in an obsidian lava flow), followed by further kinetic fractionation as the argon diffuses into the obsidian.

No empirical data for ^{36}Ar diffusivities are available to compare with that of ^{40}Ar. The abovementioned studies have used Graham's law and the kinetic theory of gases to estimate the maximum difference in diffusivities between Ar-isotopes, which provides an upper estimate of the ratio of diffusivities (0.949 for $^{40}Ar/^{36}Ar$):

$$\frac{\text{Diffusivity A}}{\text{Diffusivity B}} = \sqrt{\frac{\text{Mass of B}}{\text{Mass of A}}}$$

They noted that the co-variation of $^{40}Ar/^{36}Ar$ with $^{38}Ar/^{36}Ar$ is broadly consistent with this level of diffusive fractionation (Morgan et al., 2009). However, the kinetic theory of gases holds true for single ideal gases only; it is an approximation for diffusion of gases through air but unlikely to be fully representative of the diffusion of a gas through a silicate network. Furthermore, recent studies of the diffusion of noble gases (Amalberti et al., 2016) and other elements through silicate melts, glasses and other mineral lattice networks have identified diffusive isotope fractionation effects beyond those expected according to Graham's law (Goel et al., 2012; Richter et al., 2009, 2008, 2003; van Zuilen et al., 2016).

Identification of the fractionation processes leading to excess ^{36}Ar in obsidians and their effect on $^{40}Ar/^{36}Ar$ systematics is revealing crucial insights, but many problematic issues persist. Firstly, experimentation using a MAP 215-50 mass spectrometer (Morgan et al., 2009; Vogel et al., 2006) cannot resolve true ^{36}Ar from interfering contaminants $^{1}H^{35}Cl$ and $^{12}C_3$. In these studies ^{35}Cl measurements were not reported and it was not discussed whether measured ^{36}Ar abundances were representative of true ^{36}Ar concentrations; contaminants at mass 36 will be a particular problem for samples with low ^{36}Ar contents and for geologically young samples (as most obsidians are). Secondly, it has been proposed that Ar will diffuse into cooling obsidian because the melt Ar content is lower than that of the atmosphere, but this is problematic as the atmospheric partial pressure of Ar is extremely low at ~9.3 mbar. Ar solubility data from diffusion experiments on rhyolitic melts at high Ar partial pressures (e.g. Carroll and Stolper, 1993) indicate likely Ar insolubility at atmospheric conditions. If true, rhyolitic melt would diffusively degas any remaining Ar, rather than resorb it from the atmosphere.

Furthermore, even if extrapolation of Ar solubility from laboratory to natural conditionals were inappropriate, and Ar solubility at atmospheric pressure were non-negligible, the volume of rhyolitic melt/obsidian affected by atmospheric Ar resorption would be strongly limited by the diffusion rate of Ar in silicate melts and glasses. In order for significant diffusive resorption to occur, an unrealistic path length may be required (for equivalent arguments for H_2O diffusive degassing from fragmented rhyolitic melt see Castro et al., 2012). Fig. 2 illustrates Ar diffusion profiles calculated for diffusion of Ar into obsidian at temperatures from 850 °C (a typical extrusion temperature) to 550 °C. The diffusion profiles were calculated using Fick's second law, and assuming an Arrhenian relationship with an activation energy (E) of 144 kJ mol^{-1} and a pre-exponential factor (D_0) of -6.16 m^2 to calculate diffusivity (D) at different temperatures (Behrens, 2010a, 2010b; Carroll and Stolper, 1991; Carroll, 1991). Even if negligible cooling occurred over ten days, Ar diffusion would only affect the outer ~1 mm of lava surfaces (the upper carapace, plus fractures and bubbles that are permeably connected, Castro et al., 2012).

Constraints on the cooling rate of natural obsidian within lavas or pyroclastic material are predominantly gained via relaxation geospeedometry, where the thermal behaviour of the sample around the glass transition temperature (~600–700 °C) is used to reconstruct its initial rate of cooling (e.g. Gottsmann and Dingwell, 2001). Published results

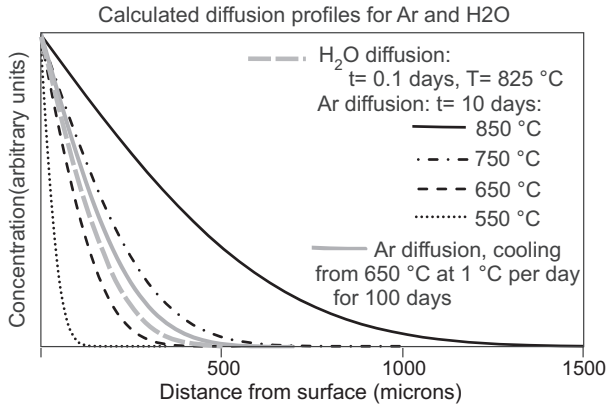

Fig. 2. Calculated concentration profiles for Fickian diffusive gain of water (Castro et al., 2005) and Ar in obsidian. Ar diffusion parameters: $E = 144\ kJ\ mol^{-1}$, $\log D_0 = -6.16\ m^2\ s^{-1}$ and assuming a spherical geometry (Behrens, 2010b; Carroll and Stolper, 1991; Carroll, 1991). It takes 10 days at eruption temperatures for Ar to diffuse the same distance as water in ~2 h.

display considerable variability, both between and within individual lava bodies, ranging from 1 to over 100 K per day (Gottsmann and Dingwell, 2002, 2001; Seaman, 2013; Wilding et al., 1995). This was demonstrated for an obsidian lava on Lipari, Italy where the upper and lower margins of a flow ramp cooled at > 140 °C per day, while the inner core cooled at only ~59 °C per day (Gottsmann and Dingwell, 2001). There is thus generally a coincidence between the portions of a lava body that cooled the most rapidly and those most likely to have interacted with the atmosphere, due to greater proximity to cooling surfaces. Thus, portions of obsidian most likely to interact with air will be those that have shorter lengthscales for diffusive Ar uptake. Plausible cooling timescales within the temperature range over which significant Ar diffusion occurs (erupted at 750–900 °C and cooling to ~500 °C) are therefore in the range 2–500 days. It is therefore unlikely that temperatures in lava flows would be maintained sufficiently long to produce diffusion profiles exceeding a few hundred microns in length. This is especially true for the model of Brown et al. (2009) where the presence of a crack formed in the brittle regime requires the obsidian to have already cooled below the glass transition temperature of ~600–700 °C e.g. (Seaman, 2013). In reality, ephemeral fracture systems may develop in obsidian above T_g (Tuffen et al., 2003), and bubble growth above T_g may also provide permeable pathways for fluid escape or ingress (Stasiuk et al., 1996). Nonetheless, the spatial extent of Ar diffusion is severely limited, and far less than that of faster-diffusing water (Fig. 1).

Consequentially, only a small proportion of the total volume of obsidian is likely to have diffusively exchanged Ar with the atmosphere, which challenges models of atmospheric Ar contamination of obsidian. As $^{40}Ar/^{39}Ar$ analysis is typically conducted on chips of fresh, non-hydrated obsidian far from exposed surfaces, connected bubbles and pervasive fractures, there is generally little scope for significant post-eruptive Ar diffusion into measured samples.

Evidently, large gaps in our understanding of the $^{40}Ar/^{39}Ar$ systematics in obsidian remain, which need to be addressed before robust age determination is possible. Many of these problems are exacerbated by the fact that obsidians are usually geologically young, being metastable supercooled fluids that seldom persist beyond a few millions of years before converting to devitrified crystalline assemblages. The low abundance of radiogenic $^{40}Ar^*$ in such young samples results in greater uncertainties in the $^{40}Ar/^{39}Ar$ system than in older samples.

2. Sample and methodology

Obsidian from Cochetopa Dome (San Juan, USA) is some of the oldest known on Earth (~27 Ma; (Lipman and McIntosh, 2008)) and forms fresh-looking nodules (perlitic beads/"apache tears"), surrounded by a hydrated matrix, and extensively devitrified, flow-banded material. Cochetopa dome samples thus afford an excellent opportunity to make detailed measurements on fresh, hydrated and devitrified obsidian, in material sufficiently old to reasonably resolve radiogenic $^{40}Ar^*$ from trapped ^{40}Ar. Sample OOL-31A was previously analysed by Lipman and McIntosh (2008) by laser stepped heating of fresh obsidian from the cores of large, fresh perlite beads and gave a plateau age of 26.9 ± 0.1 Ma (1 standard deviation), using the decay constants and isotope abundances of Steiger and Jäger (1977) and a Fish Canyon Sanidine fluence monitor age of 28.02 Ma (Renne et al., 1998). The Cochetopa Dome extruded within the Cochetopa Caldera; little palaeonvironmental evidence has been presented for this eruption, but it's eruption within an actively subsiding caldera filled with tuffs and volcaniclastic sediments (Lipman and McIntosh, 2008) suggests that this obsidian formed either subaerially, or perhaps in contact with caldera lake water.

Polished slabs were prepared from a piece of variably devitrified flow banded obsidian and from a 17 mm diameter fresh perlite bead selected from Sample OOL-31A (Fig. 3). The fresh perlite bead is transparent with faint flow bands displayed as subtle variations in colour and translucency. The variably devitrified slab displays a range of textures: flow banding in the freshest parts of the obsidian is seen as alternating light and dark bands of varying thickness and opacity running across the sample, related to variable number densities of microlites. Discontinuous bands of opaque, amorphous pink and grey material are interpreted as devitrified patches and are elongate sub-parallel to the flow bands in the fresh material. They represent spherulitic growth that originated from chains of band-parallel nuclei and are fringed by overgrowths displaying sharp, undulose and locally feather-like contacts with the surrounding glassy material. The glass is

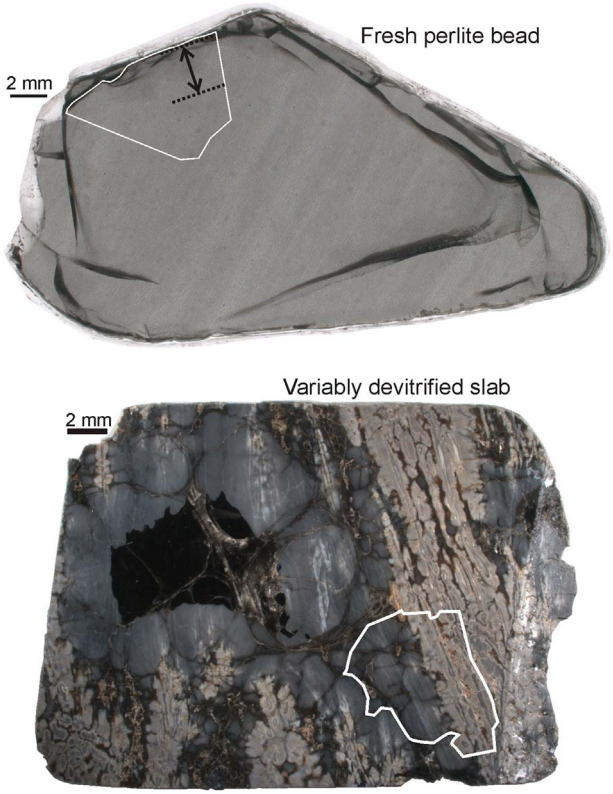

Fig. 3. Photographs of polished slabs of the large, fresh perlite bead and the variably devitrified flow banded obsidian. White lines show the fragments selected for UV-LAMP Ar-isotope analysis. On the fresh perlite bead, the dotted black lines show the positions of the innermost and outermost laser ablation trenches.

cut by a high density of concentric, curved perlitic cracks, which break up the fresh obsidian into small (1–7 mm) perlitic beads. The smallest beads are spatially associated with the most highly devitrified patches.

2.1. Ar-isotope analysis

300 μm-thick polished slabs were demounted and small (1 cm^2) fragments from each of the slabs were selected for Ar/Ar analysis, washed with acetone and deionised water, packaged in Al-foil, loaded into a foil tube and irradiated at the McMaster Reactor (Canada) for 16.7 h using cadmium shielding. The neutron flux was monitored using biotite standard GA1550, grains of which were loaded into 1 cm foil packets and distributed throughout the irradiation tube. Grains from each packet were analysed by single grain fusion and J-values for each slab fragment were calculated by linear extrapolation of J-values between standards within the irradiation tube. J-values were calculated assuming an age of 98.79 ± 0.96 Ma (Renne et al., 1998) which is consistent with the fluence monitor age used by Lipman and McIntosh (2008) to allow direct comparison of our new $^{40}Ar/^{39}Ar$ data with theirs. A New Wave Research Ltd. LUP 213 nm, 20 mJ, pulsed Nd-YAG laser was used to ablate trenches across the polished surfaces of the slabs at 20 Hz and 65% power. The geometry of the trenches was texture-dependent and ranged from 0.3 mm^2 rasters to trenches 100 μm wide and up to 6 mm long. Lasering durations were typically 8 min. Significant redeposition of ablation ejecta was not observed via the optical camera attached to the laser system. Unwanted gas species were removed from released gases by two SAES getters, one operating at room temperature and the other at 450 °C, for a minimum of 150 s prior to automatic inlet into a Nu Instruments Noblesse mass spectrometer, which is able to resolve ^{36}Ar from $^{36}(C_3)$. Masses 35, and interfering peak shoulders on the high mass sides of masses 36 (36-high) and 39 (39-high) were measured in addition to the Ar isotopes to monitor for chlorine and hydrocarbon interferences, respectively. No correlation between blank corrected ^{36}Ar and blank corrected 36-high or ^{35}Cl was observed (Fig. 4), suggesting that apparent ^{36}Ar abundances have not been artificially increased by contamination from hydrocarbon or $^{36}(HCl)$ mass interferences. Blanks were measured between each sample analysis. All data were corrected for blanks, ^{37}Ar decay and neutron-induced $^{40}Ar_K$, $^{39}Ar_{Ca}$ and $^{36}Ar_{Ca}$. Atmospheric ^{40}Ar calculations were carried out assuming an atmospheric argon composition of $^{40}Ar/^{36}Ar = 295.5$ (Steiger and Jäger, 1977). All errors quoted in tables and text are 1 standard deviation unless otherwise stated. We note the existence of an updated value for the composition of atmospheric Ar (Lee et al., 2006) and for the age of GA1550 (Spell and McDougall, 2003), but have adopted the same external correction factors as those used by Lipman and McIntosh (2008) for ease of comparison between their data and ours. A minority of analyses produced ^{36}Ar and ^{37}Ar yields that were indistinguishable from blank and where this resulted in a negative blank-corrected figure, the value was assumed to be 0 for the purpose of Ca and atmospheric corrections to the $^{40}Ar/^{39}Ar$ age. ^{37}Ar yields were low for all analyses, which is not surprising given the low CaO content (0.41%) of the sample (Lipman and McIntosh, 2008). During Ar-isotope analysis, no unusual baseline fluctuations were observed and the peak positions for low-abundance isotopes (including ^{36}Ar) were monitored to ensure that the low measured abundances were real and not the result of measuring off-peak, so these exceptionally low abundances are considered to be real and not an artefact of ablating too little material or of decay of ^{37}Ar to undetectable levels.

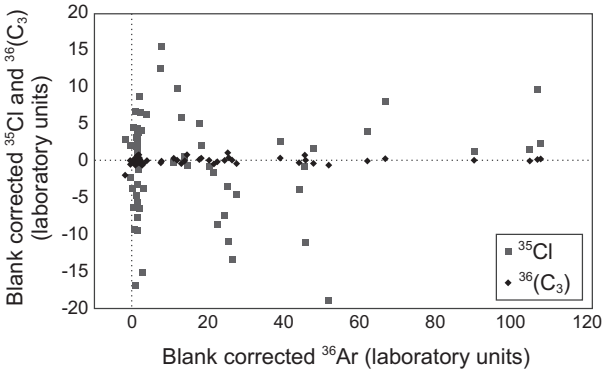

Fig. 4. Apparent ^{36}Ar yields plotted against measured ^{35}Cl and $^{36}(C3)$ to check for overestimation of ^{36}Ar due to contamination from species with an interference at mass-36. All values are blank corrected. There is no correlation between apparent ^{36}Ar yield and the potential contaminants, suggesting that the ^{36}Ar values are correct and have not been overestimated.

2.2. Infra-red spectroscopic analysis

A doubly polished wafer of ~250 μm thickness was prepared from an equivalent section of the fresh perlite bead. Unfortunately, pervasive fracturing of the devitrified sample defied all attempts to prepare doubly polished wafers. Infra-red spectroscopy was used to characterise dissolved water concentrations in the glass, using the system at Lancaster University (Thermo Nicolet IR interferometer with KBr beamsplitter, coupled to a Continuum Analytical microscope, with an MCT-A detector and 50 μm square aperture). 128 spectra were collected in the mid-IR range of 4000–1000 cm^{-1}. Twelve-point linear baseline corrections were used to quantify the H_2O_t absorption peak at 3550 cm^{-1}, and peak values were converted to species concentrations using the Beer-Lambert Law and a glass density of 2300 kg m^{-3}. A Mitutoyo digital micrometer was used to measure wafer thickness, with an accuracy of ± 3 μm, and an absorption coefficient of 80 $lmol^{-1}$ cm^{-1} was used for the 3550 cm^{-1} peak (Newman et al., 1986). The combined absolute uncertainty on such IR measurements is ~10%, with significantly smaller relative errors (e.g. von Aulock et al., 2014).

3. Ar/Ar results

3.1. Fresh perlite bead

The fresh perlite bead was analysed by measuring the gas released from a series of 22 trenches excavated between the rim and the core of the bead. The analyses gave apparent Ar ages between 25.80 ± 0.57 and 26.99 ± 0.52 Ma. Eight of these analyses are within one standard deviation of Lipman and McIntosh's (2008) published age (26.91 ± 0.1 Ma) and all are within two standard deviations. There does not appear to be any systematic variation between the ages with distance from the bead rim. A weighted average of all 22 data points (excluding the error on the J-value) gives an age of 26.59 ± 0.06 (1 s.d.) with an MSWD (mean square of weighted deviates) of 0.37 and a probability of 0.996. An inverse isochron diagram of all data excluding the three analyses that did not yield ^{36}Ar above blank (n = 19) gives an age of 26.61 ± 0.17 Ma with a trapped $^{40}Ar/^{36}Ar$ of 283 ± 33, an MSWD of 0.41 and a probability of 0.98. The trapped $^{40}Ar/^{36}Ar$ value is indistinguishable from that of air and the large error on the intercept is due to clustering of the data at the radiogenic end of the isochron diagram. The weighted average and the isochron age are indistinguishable and we adopt the more precise age of the weighted average. Recalculating the weighted average to include the error on the J-value gives an age of 26.58 ± 0.07 Ma. This age is 330 ka younger than the previously published age.

Distribution of K (as ^{39}Ar) and ^{36}Ar throughout the bead were investigated by normalising ^{39}Ar and ^{36}Ar to ^{37}Ar and plotting against rim-core distance. ^{37}Ar was chosen as the normalising factor as it is derived from Ca, which should remain immobile during hydration of the volcanic glass, although the low abundance of Ca in the sample results in relatively large errors on the ^{37}Ar values and subsequent

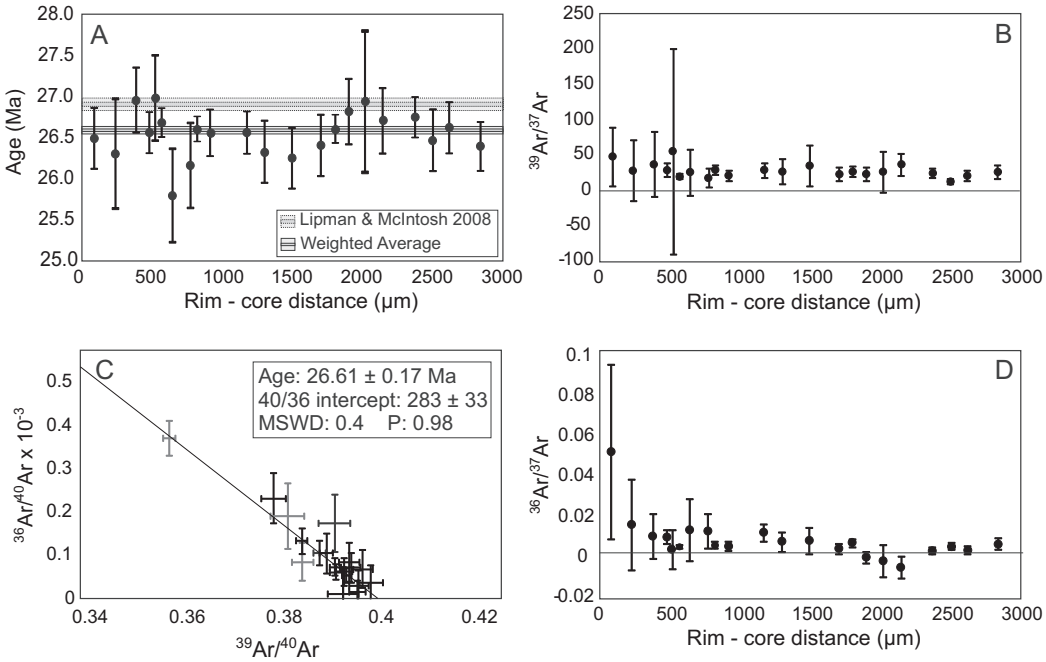

Fig. 5. Ar-isotope and age data for the fresh perlite bead. A: Apparent Ar-age with distance from the bead rim. Data point error bars are one standard deviation. Dark and light boxes for the weighted average and published ages represent one and three standard deviations. B: Spatial distribution of K plotted as ^{39}Ar/^{37}Ar. C: Inverse isochron diagram of the 19 data points that yielded ^{36}Ar measurements above blank. Grey error bars represent the three analyses closest to the rim. D: Spatial distribution of ^{36}Ar normalised to ^{37}Ar; negative values are an artefact of exceptionally low ^{36}Ar yields and analyses being indistinguishable from blank. Larger isotope ratio errors near the rim of panels B and D are due to larger proportional errors on the ^{37}Ar analyses.

ratios. ^{39}Ar showed very little variation with distance from the bead rim, indicating a uniform K:Ca ratio throughout the perlite bead. ^{36}Ar also appears uniform throughout the bead except for the outer few hundred microns where elevated ^{36}Ar/^{37}Ar values occur. These values are associated with higher errors; ^{37}Ar analytical errors are proportionally larger in the first few analyses, due to smaller overall signal sizes while the optimum ablation length was being determined, and these errors propagate through to create larger errors on the isotope ratios. Elevated ^{36}Ar is also reflected in significantly lower radiogenic ^{40}Ar (^{40}Ar*) yields in the outer few hundred microns (Fig. 5), as ^{40}Ar* is calculate by subtracting atmospheric ^{40}Ar (calculated based on measured ^{36}Ar) from the total measured ^{40}Ar.

3.2. Variably devitrified slab (fragment H)

Ar-isotopes were characterised for a number of discrete textural zones on the devitrified slab. The core-rim variation of three small perlite beads (A–C) was investigated by excavating concentric trenches in each bead. Flow banding in relatively fresh obsidian was investigated in a fourth small perlite bead (D) by rastering across areas of ~0.3 mm^2. Visually distinct bands and patches in the highly devitrified material were analysed by ablating trenches ~100 μm wide or rastering across areas up to 0.5 mm^2. The textural context and position of the analyses and a summary of the data as Ar/Ar ages is given in Fig. 6.

Highly devitrified material, appearing as flow bands and patches of opaque pink and grey material, gives a range of ages (24.09 ± 2.89 to 29.42 ± 1.45 Ma), most of which are slightly younger than the fresher material (Fig. 6). These patches yielded the highest ^{36}Ar/^{37}Ar values (0.14 ± 0.03 to 0.72 ± 0.55) and lowest ^{39}Ar/^{37}Ar values (5.7 ± 1.27 to 17.17 ± 9.47) of the sample, indicating loss of K and high levels of non-radiogenic Argon. An isotope correlation diagram of these phases gives an age of 25.6 ± 1.2 with a ^{40}Ar/^{36}Ar intercept of 298.6 ± 6.3, an MSWD of 2.2 and a probability of 0.086.

The three small beads have diameters of 1.7 (bead A), 0.8 (bead B) and 1.4 (bead C) mm (Fig. 5). All three beads exhibit slight age gradients with age decreasing from rim to core. ^{39}Ar/^{37}Ar values show

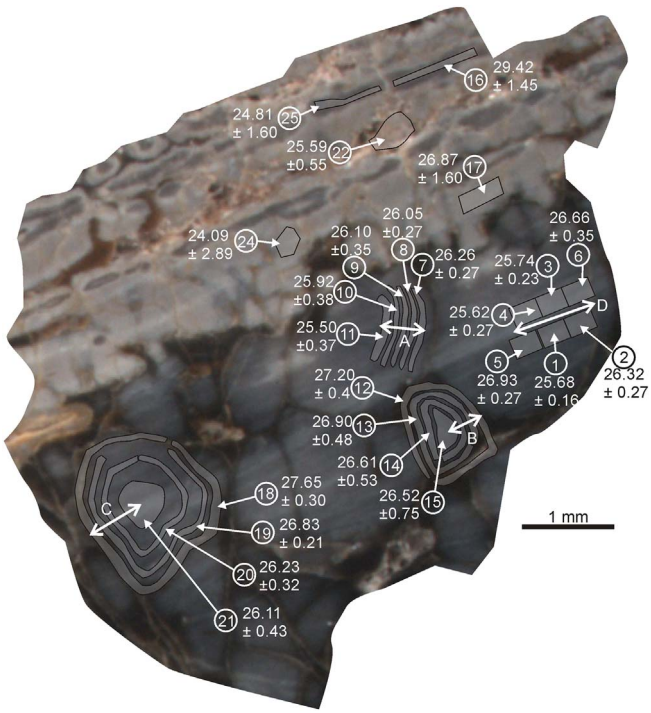

Fig. 6. Fragment H of the polished slab showing the location and context of Ar-isotope analyses. A colour image is available in the online version of the article.

no systematic variation with distance from the bead rim, and are indistinguishable from the values produced by the fresh perlite bead, suggesting a uniform K-content (Fig. 7).

Bead A produced ages between 25.5 ± 0.37 and 26.26 ± 0.27 Ma. All of the ages are younger than the age of the fresh perlite bead, but are within three standard deviations of the weighted average. An inverse isochron plot (n = 5) gives an age of

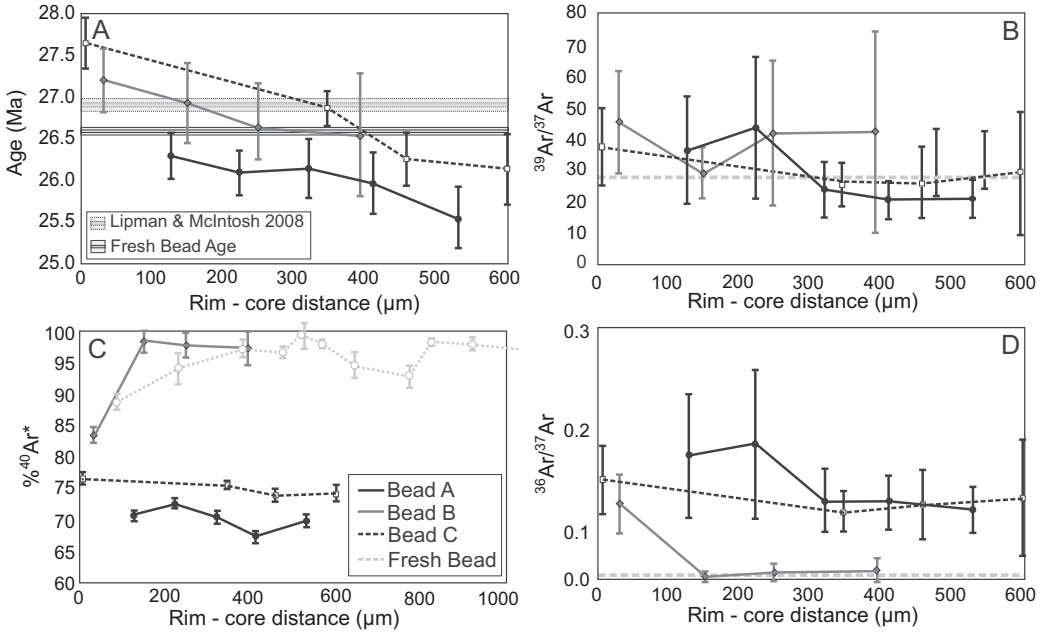

Fig. 7. A: Core-rim age variation in the 3 perlite beads compared to the weighted average age of the fresh perlite bead and Lipman and McIntosh's published age. B: Core-rim variation in ^{39}Ar/^{37}Ar as a proxy for K:Ca. Grey dashed line is the average value of the fresh perlite bead and is shown as a rough comparison only as the neutron fluence (i.e. ^{37}Ar production) is slightly different between slabs – see Supplementary Data for J-values. C: Core-rim variation of ^{40}Ar* yield compared to the outer 1 mm of the fresh perlite bead. D: Core-rim variation in ^{36}Ar/^{37}Ar compared to the average value of the inner portions of the fresh perlite bead (grey dashed line).

25.8 ± 2.4 Ma with a ^{40}Ar/^{36}Ar intercept of 300 ± 50, an MSWD of 1.0 and a probability of 0. ^{36}Ar/^{37}Ar values are higher than for the fresh perlite bead, with the highest values occurring in the outermost part of the bead. This elevated ^{36}Ar is mirrored by relatively low ^{40}Ar* yields (calculated based on measured total ^{40}Ar and ^{36}Ar) of ~70%.

Bead B produced ages between 26.52 ± 0.75 and 27.2 ± 0.4 Ma. All of the ages are within error of the weighted mean age of the fresh perlite bead but the analyses closer to the rim are older, while the core analyses are almost exactly the same as the fresh bead weighted average (Fig. 7). An inverse isochron plot gives an age of 26.67 ± 0.85 Ma with a ^{40}Ar/^{36}Ar intercept of 325 ± 68, an MSWD of 0.117 and a probability of 0.89. $N = 4$, but three of the data points are clustered and the trend of the isochron line is controlled by the high ^{36}Ar analysis closest to the rim. Most of the ^{36}Ar/^{37}Ar values are comparable to that of the fresh bead apart from the analysis closest to the rim which exhibits a higher level of ^{36}Ar and a corresponding lower ^{40}Ar* yield (Fig. 7).

Bead C produced apparent ages between 26.11 ± 0.43 and 27.65 ± 0.3 Ma. This age range spans the weighted average of the fresh perlite bead but the outermost analysis is significantly older. An inverse isochron diagram shows that the Ar-isotope system in this bead is clearly disturbed as it gives an apparent age of 46 ± 140 Ma with a ^{40}Ar/^{36}Ar intercept of −373 ± 470, an MSWD of 0.67 and a probability of 0.51. ^{36}Ar/^{37}Ar values are higher than for the fresh perlite bead and ^{40}Ar* yields are lower.

The fourth small bead (bead D, 2 mm diameter) was analysed to investigate any isotopic difference between dark and light (translucent) coloured flow bands. The light coloured flow bands were glass that appeared clear in thick section and relatively free from microlites and inclusions, while the dark flow bands appeared black in the thick section due to an abundance of microlites. Core-rim variation within each flow band was investigated by analysing 3 rastered trenches per flow band. Both flow bands give similar age ranges but the light flow band shows a progression of an older age (26.66 ± 0.35 Ma) at the rim to a younger age (25.62 ± 0.27 Ma) at the core, while the dark band does not show a systematic variation of age with core-rim distance (Fig. 8). ^{39}Ar/^{37}Ar values show no variation. The light flow band has a higher ^{36}Ar content, with higher ^{36}Ar/^{37}Ar values showing a slight increase towards the core and lower ^{40}Ar* yields (decreasing from 86% at the rim to 78% in the core) compared to the dark flow band. ^{36}Ar yields are slightly higher (albeit within error due to low abundances of ^{36}Ar and ^{37}Ar) at the core compared to the rim in the dark flow band and the core-rim variation is much less than in the light flow band (Fig. 8).

4. Water concentration results

Water concentration data in an equivalent section through the fresh perlite bead are shown in Fig. 9, along with an image of the wafer in order to show the relative positions of the data points. The interior of the bead shows a remarkably homogenous water concentration, with mean of 0.22 ± 0.01 wt% ($n = 102$, 1 standard deviation), and range 0.20–0.23 wt%. By contrast, there is strong H_2O enrichment within the outer 200 μm of one side of the wafer, reaching 0.68 wt% in the outermost analysis directly adjacent to the bead-bounding fracture. An equivalent enrichment could not be determined on the other side of the traverse due to an irregular wafer edge, which prevented reliable H_2O determination.

5. Discussion

5.1. Obsidian texture and water content

The low water content of the interior of the fresh perlite bead is consistent with degassing to near-atmospheric conditions, and thus almost complete loss of the magmatic H_2O component (e.g. Friedman and Smith, 1958). The elevated water content at the rim indicates strong but spatially-localised hydration, which is consistent with diffusion of H_2O having advanced approximately 200 μm into the perlitic bead. This distance is consistent with other studies that have quantified H_2O diffusion signatures in perlitised obsidian (Tuffen et al., 2010; von Aulock et al., 2013), albeit in far younger samples that have interacted with high-temperature aqueous fluids over far shorter timescales. We thus interpret this obsidian to have degassed the majority of its magmatic volatiles during eruption and to have undergone limited post-eruption hydration at the margins of perlite bead rims.

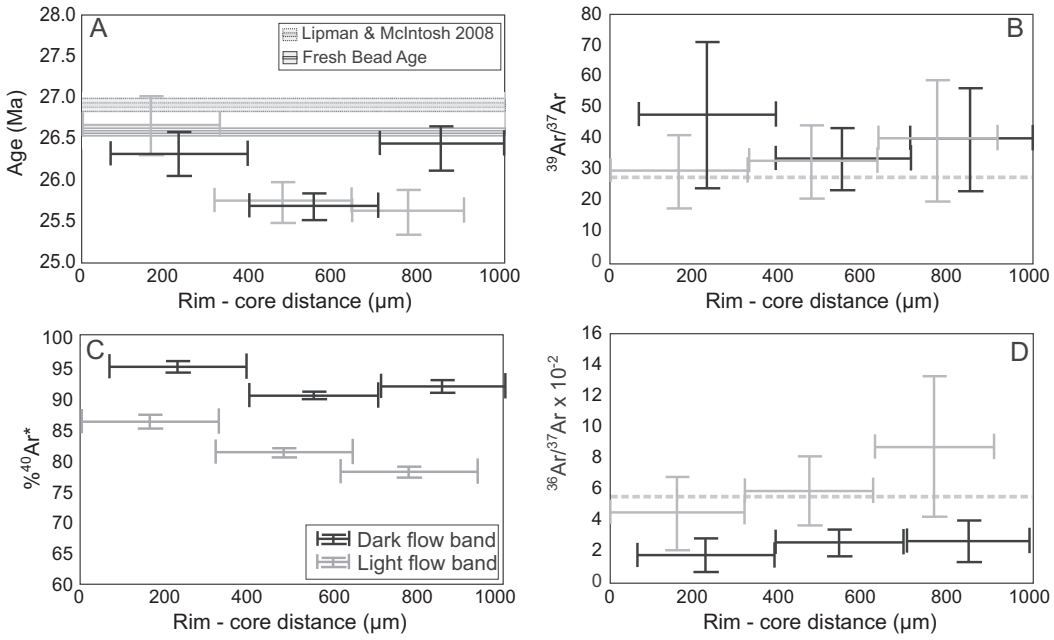

Fig. 8. A – Rim to core Ar-age profiles of the two flow bands in perlite bead D, compared to the weighted average of the fresh perlite bead and Lipman and McIntosh's age. B – Rim-core $^{39}Ar/^{37}Ar$ values as a proxy for K content. The bead shows no systematic variation and is indistinguishable from the average value of the fresh perlite bead. C – Rim-core variation in radiogenic ^{40}Ar yield. Both flow bands show a decrease in radiogenic yield towards the core, consistent with diffusive loss of initial Ar from the bead rim by degassing during cooling. D – Rim to core variation in ^{36}Ar (normalised to ^{37}Ar as a proxy for Ca) compared to the average value for the core of the fresh perlite bead (rough approximation – see Fig. 7).

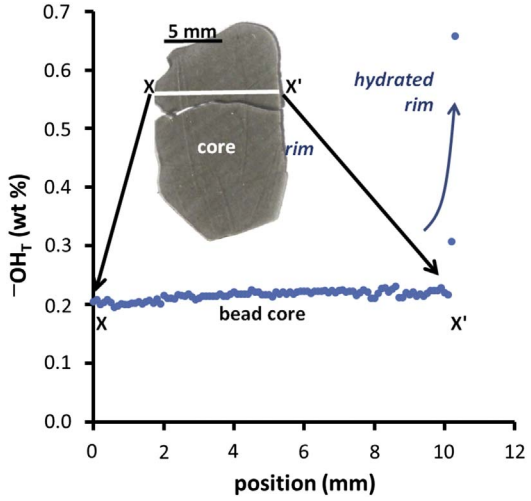

Fig. 9. Spatial variation in water content across the fresh perlite bead. Elevated water contents are present in the right hand rim of the bead. The left hand rim of the bead appears broken and the hydrated rim may have been lost during sample preparation.

Water concentrations are not available for Fragment H, but the presence of both perlitic textures and strongly devitrified bands indicates the involvement of water mobility in the alteration process. It is well established that perlitised obsidian displays elevated H_2O concentrations (e.g. Denton et al., 2012; Ross and Smith, 1955; von Aulock et al., 2013), with D/H ratios indicating ingress of meteoric water (Bindeman and Lowenstern, 2016). Additionally, the growth of anhydrous mineral assemblages during devitrification, e.g. spherulites, creates diffusive fronts of magmatic volatiles that flux through the surrounding obsidian (Castro et al., 2008; Gardner et al., 2012; von Aulock et al., 2013). The latter process can therefore liberate and concentrate a magmatic H_2O component that can then be resorbed during obsidian cooling and hydration. This conflicts with the traditional model that hydration involves uniquely meteoric water (e.g. Ross and Smith, 1955). Indeed, models of the textural evolution of obsidian flows describe how crystallisation of anhydrous phases within flow interiors liberates magmatic H_2O, which migrates and resorbs into the upper part of the flow, driving vesiculation (Manley and Fink, 1987). These vesicles may, in turn, act as nucleation points for spherulite growth (Seaman, 2013), which then promotes further magma H_2O mobility. Increased H_2O solubility during cooling of obsidian promotes retrograde water resorption and enrichment, with H_2O derived from either magmatic or meteoric sources (Ryan et al., 2015). The textures in Fragment H thus reflect the higher volatile content of this obsidian than the fresh bead, with volatile enrichment either reflecting ingress of magmatic volatiles locally liberated by devitrification, absorption of meteoric water and other volatiles due to retrograde solubility during cooling, less efficient degassing of magmatic volatiles, or any combination of these three mechanisms.

5.2. Spatial variation in Ar-isotopes

Ar-isotopes show significant spatial variation within and between different obsidian textures and microtextures. In many cases, these observations are not consistent with simple binary mixing between radiogenic and a trapped end-members – a condition necessary for robust $^{40}Ar/^{39}Ar$ dating. Key observations of Ar-isotope distribution are:

1. The low ^{36}Ar content (using $^{36}Ar/^{37}Ar$ as a proxy) of the fresh perlite bead interior and Bead B of Fragment H (Figs. 5 and 7).
2. The higher ^{36}Ar content at the rim of the fresh perlite bead and Bead B of Fragment H (Figs. 5 and 7).
3. Lower $^{40}Ar^*$ yields in the outer few hundred microns of the fresh bead and Bead B (Fig. 7).
4. Decreasing apparent $^{40}Ar/^{39}Ar$ age from rim to core in the perlite beads of Fragment H (Figs. 6 to 8).
5. The difference in ^{36}Ar content between the dark and pale flow bands in Bead D of Fragment H (Fig. 8).
6. The decrease in $^{40}Ar^*$ yield from rim to core in the pale flow band of Bead D in Fragment H (Fig. 8).
7. The increase in ^{36}Ar content (using $^{36}Ar/^{37}Ar$ as a proxy) from rim to core in the pale flow band of Bead D (Fig. 8).
8. The range in different proportions of radiogenic to trapped argon

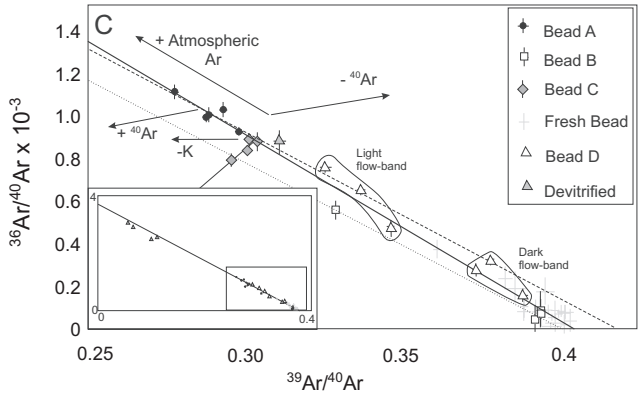

Fig. 10. Inverse isochron diagram showing the relationship of the various obsidian microtextures and the expected data trajectories that would be produced by changes to the Ar-isotope system. Inset shows the full range of data points with the isochron line for the fresh perlite bead. The boxed area on the inset shows the extent of the main diagram, which is expanded to include more detail while excluding four of the devitrified analyses. The thick, solid line is the isochron for the large fresh bead, dashed line is the isochron for Bead A, dotted line is the isochron for Bead B and thin solid line is the isochron for Bead C.

between perlite beads in Fragment H (Fig. 10).

Below, we discuss possible mechanisms that could generate these observations, in the context of the textural and volatile interpretations above, to derive hypotheses for the volatile and Ar-isotope evolution of these samples.

As previously discussed, mixing between radiogenic argon and multiple reservoirs of trapped argon (e.g. an atmospheric and an excess ^{40}Ar component, or multiple excess ^{40}Ar components) have the potential to produce statistically robust, but meaningless isochrons (Flude and Storey, 2016; Kuiper, 2002; Sherlock and Arnaud, 1999). Fig. 10 plots the obsidian data on an isotope correlation diagram and shows the expected trajectories that data points would follow if the Ar-isotope system were disturbed by loss of ^{40}Ar, loss of K, addition of atmospheric argon, or addition of excess ^{40}Ar. Much of the spread in data between different obsidian textures can be superficially explained by mixing between a radiogenic end-member and different proportions of trapped argon with a roughly atmospheric composition. The fresh perlite bead plots at the radiogenic end of the isotope correlation diagram, along with Bead B and the dark flow band from Bead D. The least radiogenic data come from the strongly devitrified areas.

5.3. Argon reservoirs

In the case of the fresh perlite bead and Bead B, much of the Ar-isotope data appears to be radiogenic (Fig. 10). The variation in Ar-isotopes correlates with water content, with higher proportions of ^{36}Ar and higher water concentrations occurring in the outer 400 and 200 μm, respectively. The low proportion of non-radiogenic argon in the interior of the fresh bead is consistent with the interpretation, based on water concentration, that this sample is well degassed from its magmatic volatiles. The coincidence of elevated water and ^{36}Ar content in the fresh bead suggests that, in this case, obsidian hydration causes an overprinting of atmospheric argon into the regions of obsidian affected by hydration. The consistent apparent ^{40}Ar/^{39}Ar age across the fresh bead suggests that this overprinting does not cause Ar-isotope fractionation, and unfractionated atmospheric argon is incorporated. In this case, we interpret the non-radiogenic component as secondary argon introduced to the obsidian from an external water source at some point after extrusion (Cerling et al., 1985).

In the case of perlite bead D, the dark, microlite-rich flow band gave a lower ^{36}Ar yield than the light flow band. The light flow band is glass clear and appears to be very fresh, while the dark flow band is more opaque due to the presence of microlites. Closer inspection of Fig. 6 shows that Bead B, which is also interpreted to be well degassed, formed in the same dark flow band as sampled in Bead D. This observation shows that significant variation in the proportion of non-radiogenic argon can occur in a sample due to microtextural differences at the hundreds of microns scale. If this variation is due to simple mixing between different proportions of two argon reservoirs (radiogenic and trapped) then it should be possible to derive reliable ^{40}Ar/^{39}Ar ages. If, however, fractionation or multiple trapped argon reservoirs are involved, deriving a reliable ^{40}Ar/^{39}Ar age will not be possible. There are two likely mechanisms to produce the variation in ^{36}Ar content between the different flow bands. The first is that the dark flow band underwent a greater degree of degassing of initial magmatic volatiles, enhanced by and/or promoting the formation of microlites. In this case, the initial magmatic argon will have contained a component of air-derived argon, perhaps due to assimilation of hydrothermally altered rocks in the magma chamber or by exchange with hydrothermal fluids (see below). The second mechanism draws on the observation that there appears to be a rough correlation between non-radiogenic argon and proximity to the devitrified area (Figs. 6 and 10). This is consistent with volatile expulsion from the devitrifying (pink and grey) zone, as described above (c.f. (Gardner et al., 2012; Manley and Fink, 1987)), resulting in an enrichment of volatiles in the region surrounding the devitrified zone. This subsequent volatile enrichment may have caused cracking and perlite formation in the surrounding obsidian.

5.4. Obsidian argon degassing profiles

All of the perlite beads in Fragment H show variation in apparent ^{40}Ar/^{39}Ar age, with ages decreasing from rim to core. This age pattern cannot be explained by diffusive loss of ^{40}Ar* from the bead rims over geological time, as this would produce younger rims and older cores. Older ages at bead rims are consistent with diffusive uptake of excess ^{40}Ar during interaction with an external excess ^{40}Ar rich-fluid or melt (Kelley, 2002). Flushing of excess ^{40}Ar-bearing gas through the lava may occur during eruption close to the vent area, but this is likely to occur at near-atmospheric pressure. As discussed above, argon solubility at low pressures in silicate melts and glasses is low, therefore high concentrations of argon would need to be present in the gas phase for this to partition into the obsidian via simple diffusion. Carbon dioxide accumulations at Sheep Mountain and McElmo Dome, located east and west of the San Juan Mountains, respectively, are derived from magmatism associated with the Colorado Plateau uplift and contain maximum concentrations of 0.02% and 0.33% ^{40}Ar, respectively (Gilfillan et al., 2008). These are comparable to ^{40}Ar concentrations of up to 0.37% in volcanic gases escaping from the base of Mount Etna (Paonita et al., 2012). Concentrations of argon in magmatic gas are thus much lower than the atmospheric concentration of argon (0.9%, Ozima and Podosek, 2002) and so post-eruptive uptake of excess ^{40}Ar by obsidian from magmatic gas, through simple diffusion, is unlikely to significantly increase dissolved ^{40}Ar concentrations. However, hydration of the obsidian by a fluid containing excess ^{40}Ar, as may happen if the hydrating fluid is magmatic or has been interacting with old, K-rich continental crust, may provide a mechanism to incorporate excess ^{40}Ar into the perlite bead rims. In this scenario, we would expect a spike in ^{40}Ar/^{39}Ar age and ^{40}Ar*% at the hydrated rim of the bead, with consistent values throughout the bead interior, or a more gentle decrease and plateau if temperatures are high enough to allow diffusion of Ar through the obsidian silicate network after hydration. Instead, gentle ^{40}Ar/^{39}Ar age gradients are observed throughout the small perlite beads, from core to rim, and ^{40}Ar* yields are either consistent across the bead, or show a decrease at the rim (Bead B, Fig. 7), suggesting addition of atmospheric argon during hydration. The only data set that shows a decrease in ^{40}Ar* yield from rim to core is from the pale flow band of Bead D, but this correlates with an increase from rim to core in ^{36}Ar yield (Fig. 8).

This variation in ^{36}Ar yield is best explained by loss of ^{36}Ar from the bead margins; it is difficult to envisage a scenario where ^{36}Ar is preferentially added to the core of a bead. This would suggest that this ^{36}Ar data represents a degassing profile that is not observed in the dark flow band because this has already more efficiently degassed. If such degassing took place without isotope fractionation, the result would simply be variable proportions of nonradiogenic argon and, assuming the trapped argon isotopic composition is well known, all analyses should give consistent ages. However, this is not observed for the pale flow band in Bead D, or for the other perlite beads in Fragment H.

As previously discussed, Ar-isotope fractionation during diffusion has been cited as a possible mechanism for producing age variation in obsidian and specifically for the low (< 295.5) $^{40}Ar/^{36}Ar$ trapped Ar compositions that have been determined by various authors (Brown et al., 2009; Morgan et al., 2009; Vogel et al., 2006). In these scenarios, incomplete equilibration of the obsidian with Ar-bearing air/water is suggested as way of increasing the $^{36}Ar/^{40}Ar$, ratio, as diffusion of lighter ^{36}Ar will outstrip that of ^{40}Ar, resulting in excess ^{36}Ar. These studies have focussed on Ar gain by cooling obsidian, but have not considered similar fractionation during diffusive Ar loss during degassing. In such a scenario, the faster rate of ^{36}Ar diffusion may lead to preferential ^{36}Ar loss, resulting in a trapped Ar composition of $^{40}Ar/^{36}Ar > 295.5$. This mechanism may thus be the cause of the excess ^{40}Ar found in some obsidians (e.g. Flude et al., 2010).

Better quantification of the different diffusivities of Ar-isotopes in silicate networks is required before such fractionation processes can be quantitatively modelled. Nonetheless, it is useful to qualitatively assess our data in terms of these fractionation models. The intercept values of the isochrons for the perlite beads all fall within error of the atmospheric Ar value, but often because the error on the intercept is relatively large, due to either relatively poor correlations or limited spread of data. As such, precise values for the composition of the trapped Ar in each perlite bead are unavailable and cannot be used to assess the presence of fractionation. However, a qualitative assessment can be made in that, when applying an atmospheric correction for trapped ^{40}Ar, excess ^{36}Ar will result in over-correction, resulting in younger ages, while excess ^{40}Ar will result in under-correction and give older ages. Beads A–D all exhibit apparently older rims and younger cores, in-keeping with our diffusive fractionation hypothesis. To further test this we plot isotope correlation diagrams for core (innermost ablation trenches – Figs. 3 and 6) and rim (outermost ablation trenches – Figs. 3 and 6) analyses from beads A–D (Fig. 11). If our hypothesis is correct we would expect the rim analyses to give an intercept indicative of excess ^{40}Ar, while the core analyses give an intercept of atmospheric composition.

An isochron of the core analyses gives an Ar/Ar age of 26.54 ± 0.64 Ma, a $^{40}Ar/^{36}Ar$ intercept of 268 ± 24, and MSWD of 0.73 and a probability of 0.53. The rim data isochron gives an Ar/Ar age of 26.5 ± 2.2 Ma, a $^{40}Ar/^{36}Ar$ intercept of 309 ± 83, an MSWD of 4.9 and a probability of 0.002 (Fig. 11). Unfortunately the poor correlations produced by scatter in the data precludes calculation of precise trapped Ar compositions. This is not surprising given the complex interplay of degassing and absorption experienced by different sized beads, all of which were presumably acting as individual domains and experienced different degrees of Ar loss and gain during degassing and absorption. Furthermore the imprecise geometric control on the plane of section of the beads inhibits precise quantitative modelling. Both intercept values are indistinguishable from the atmospheric value and each other at two standard deviations, with the poorest correlation (thus highest errors) being produced by the rim analyses which were likely subject to the most variable conditions during and after cooling of the obsidian. Nevertheless, it is clear from the isochron correlation diagram that the rim analyses trend towards a lower $^{36}Ar/^{40}Ar$ (i.e. higher $^{40}Ar/^{36}Ar$) value than the core analyses and these observations are consistent with our hypothesis.

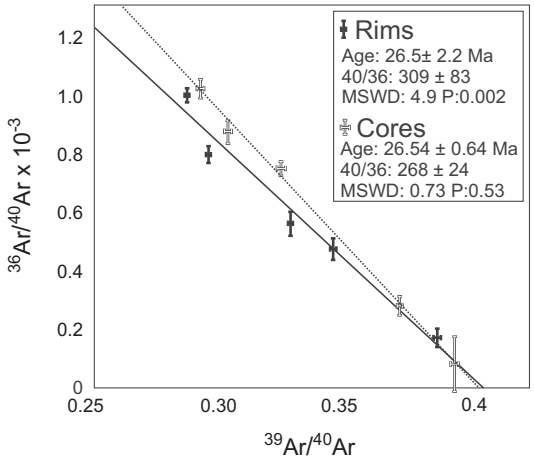

Fig. 11. Isotope correlation diagram of core (inner ablation trenches) and rim (outer ablation trenches) analyses from perlite beads A–D.

If the observed apparent $^{40}Ar/^{39}Ar$ age gradients are the result of preferential loss of ^{36}Ar during degassing, leading to a relative excess of ^{40}Ar at the bead rims, we might expect gradients in ^{36}Ar to be present in all of the affected beads, but this is only observed in Bead D. $^{36}Ar/^{37}Ar$ ratios in Beads A and C are approximately one order of magnitude higher than observed for Bead D (Figs. 7 and 8), while the rim of Bead B has a similar $^{36}Ar/^{37}Ar$ value to Beads A and C, but the interior is more similar to that of Bead D. This enrichment in ^{36}Ar at the rim of Bead B is also reflected in a lower $^{40}Ar^*$ yield at the rim, and has been interpreted as an overprinting with atmospheric argon during hydration. The lack of observed ^{36}Ar enrichment at the rim of bead D may be a sampling artefact related to the geometry of the raster pits. The elevated ^{36}Ar (and corresponding lower $^{40}Ar^*$ yields) in Beads A and C could either be due to a high initial volatile content (due to proximity to the devitrified area, postulated to expel volatiles during crystallisation), or due to later addition of argon during hydration. If the Ar-isotope composition of the perlite beads was overprinted with atmospheric argon during late-stage hydration, this would likely mask any gradients in ^{36}Ar that formed during degassing. However, adding unfractionated atmospheric argon would dilute, but not alter the apparent excess ^{40}Ar resulting from diffusive fractionation, and the apparent $^{40}Ar/^{39}Ar$ age gradients would remain.

5.5. Volcanological interpretation and lessons for $^{40}Ar/^{39}Ar$ sampling

The Ar-isotopes in this obsidian thus appear to have derived from 3 possible sources. The first is initial Ar dissolved in the melt and that remained trapped in the obsidian as it chilled. The bulk isotopic composition of this component will depend on the nature and setting of the magmatic system but can be considered to have a $^{40}Ar/^{36}Ar$ ratio of 295.5 or higher (i.e. of atmospheric composition, or containing excess ^{40}Ar). This is generally assumed to be magmatic Ar, although recent observations of explosive activity during obsidian formation open up the possibility of bulk-incorporation of atmospheric Ar into extruded melt via repeated cycles of fragmentation, adsorption and rehealing. Such fragmentation and healing cycles occur at eruptive temperatures (Tuffen et al., 2003) and lead to the transient formation of permeable pathways connecting extruding magma with the surrounding hydrothermal system (Saubin et al., 2016). We thus refer to this component, which we consider to be present in the melt phase within subaerially emplaced lava, as “initial Ar”. Poorly degassed obsidians, such as those explosively ejected from depth in the conduit as pyroclasts, should have higher trapped initial Ar contents than well-degassed melt typical of subaerial lava flows. As discussed above, this initial argon may be redistributed and concentrated within an obsidian flow by volatile expulsion from the crystallising and devitrifying flow interior. The second source is Ar from atmospheric sources incorporated

into the obsidian during or after quenching via diffusion, hydration or other alteration mechanisms; we consider this to have a bulk reservoir composition similar to that of atmospheric Ar. The third source is radiogenic $^{40}Ar^*$ derived from the radioactive decay of ^{40}K over geological timescales.

To deduce accurate $^{40}Ar/^{39}Ar$ and K-Ar ages the contribution of the first and second of these components needs to be deconvolved from the radiogenic $^{40}Ar^*$. This is usually done by assuming that all non-radiogenic Ar has an atmospheric composition, and thus correcting the ^{40}Ar value based on the ^{36}Ar yield. Any ^{36}Ar present in the obsidian is non-radiogenic, so must be derived from a trapped initial component or a post-eruption meteoric component, and so the distribution of ^{36}Ar within the obsidian may give insights into the origin of the non-radiogenic Ar and the degassing and/or absorption processes which took place in the obsidian.

The large, fresh perlite bead produced consistent $^{40}Ar/^{39}Ar$ ages and displayed a consistently low ^{36}Ar content, apart from at the rim where ^{36}Ar is elevated (Fig. 5). As discussed, this elevated ^{36}Ar at the bead rim is thought to have been introduced via hydration. The increase in ^{36}Ar without a corresponding change in apparent Ar-age suggests that non-fractionated atmospheric Ar was incorporated during hydration. The otherwise low ^{36}Ar content suggests that any initial Ar in the melt was efficiently degassed in this sample, consistent with uniformly low H_2O concentrations far from the bead margins.

In the case of perlite Bead D, the dark, microlite rich flow band gave a lower ^{36}Ar yield than the light flow band. Given the lack of alteration in the light flow band, this is consistent with a greater degree of degassing of initial Ar in the dark flow band, enhanced by and/or promoting the formation of microlites. Both flow bands exhibit lower ^{36}Ar yields towards the rim of the bead, again consistent with degassing of magmatic Ar during cooling and indicating that this perlite bead formed during an early post-eruptive phase with elevated temperatures and diffusively mobile magmatic Ar, rather than during a later devitrification event. Overprinting with atmospheric argon during hydration at the rims of Beads B and the fresh bead, and the postulated more diffuse overprinting of beads A and C indicate that a second stage of hydration took place at a later post-eruptive phase. Contrasting degassing and absorption histories appear to be present within just a few square millimetres, and these go some way to explaining the difficulties with accurately interpreting $^{40}Ar/^{39}Ar$ data from obsidians.

Fig. 12 summarises our proposed model for argon isotope evolution in Cochetopa Dome obsidian, and is used to illustrate our recommendations for selecting obsidian samples for the most reliable $^{40}Ar/^{39}Ar$ dating. We simplify argon-isotope evolution into three stages each representing the action of one of the three sources of argon, described above.

In Stage 1, the initial argon content of the melt is distributed throughout the obsidian; some parts undergo effective degassing while other areas may be enriched due to fluxing of volatiles from crystallising or devitrifying parts of the lava (Fig. 12B). Perlitic cracks form while the lava remains at high enough temperatures (> 500 °C) to promote argon diffusion through the glass structure (Fig. 12C). The perlitic cracks act as diffusion domain boundaries and argon diffuses out of the obsidian, being lost to the fast diffusion pathways at the bead rims. Degassing produces concentration gradients with depleted bead rims (Fig. 12D). Kinetic fractionation during diffusive degassing results in variable $^{40}Ar/^{36}Ar$ values across the bead with an apparent excess of ^{40}Ar (compared to air) at the rims due to preferential loss of ^{36}Ar during degassing. At the end of Stage 1, argon concentrations and isotope ratios are variable throughout the sample due to multiple degassing and enrichment pathways and variable degrees of kinetic isotope fractionation.

During Stage 2, the obsidian undergoes hydration; this introduces atmospheric argon, which overprints the initial argon isotope and concentration gradients (Fig. 12E). This may occur during the final stages of eruption, or over millions of years. Stage 3 represents the time period between chilling of the lava below ~500 °C and sample collection (in this case, ~ 27 Ma): ^{40}K radioactively decays to $^{40}Ar^*$ (Fig. 12F).

Such obsidians pose a problem for K-Ar and $^{40}Ar/^{39}Ar$ dating because of the heterogeneous initial argon content (especially in terms of isotope ratios) and because addition of atmospheric argon during hydration results in mixing of three sources of argon, making it impossible to characterise the initial component. As such, parts of obsidian that are well degassed from their initial argon, and have not experienced secondary hydration are most likely to produce reliable K-Ar and $^{40}Ar/^{39}Ar$ ages. In Fig. 12, these areas correspond to the yellow areas of panel F, and green (hydrated) and orange (poorly degassed) areas should be avoided when sampling for Ar-dating (see online version of the article for a full colour version of the figure).

5.6. Implications for volcanological study of obsidian

Quantification of Ar systematics at high spatial resolution within obsidian, when combined with their textural context within rhyolitic lava, can shed light on late-stage fluid flow and its association with crystallisation. Patterns of ^{36}Ar within small perlitic beads A-D from the partly-devitrified zone are consistent with diffusive ^{36}Ar loss at comparatively high temperatures, in contrast with the inferred lower-temperature Ar diffusion at the margin of the larger bead within fresher, non-devitrified obsidian. High-temperature fracturing of melt/glass adjacent to spherulitic masses, as seen in rhyolitic obsidian from Krafla, Iceland (Castro et al., 2008), may be driven by volumetric changes upon crystal growth, together with localised magmatic fluid overpressure. These fractures provide pathways for transport of magmatic gases that have been locally exsolved around spherulites, due to enrichment of volatiles at the boundary of the growing anhydrous crystalline assemblage.

The occurrence of fracture-driven volatile mobility associated with zones of high-temperature devitrification supports a key hypothesis about the emplacement of rhyolitic obsidian flows. The formation of late-stage pumice diapirs, prominent on the surface of many of the Holocene silicic flows in the western US (e.g. Fink, 1983), has been attributed to the release of volatiles during crystallisation of the slowly-cooling flow interior, and their transport within ephemeral fracture networks (Manley and Fink, 1987). However, spherulitic textures within US flows are only clearly found within core samples, and little evidence has been presented to date for the nature of the relic pathways that facilitated gas transport away from zones of spherulite crystallisation.

6. Implications and conclusions

UV-LAMP Ar-isotope data from a range of obsidian microtextures within a single sample, are consistent with the presence of three separate reservoirs of argon in the obsidian (initial argon, atmospheric argon introduced during hydration, and $^{40}Ar^*$), which were incorporated and modified during different phases of the emplacement and initial cooling of obsidian lava, together with later low-temperature, post-eruptive processes. Deconvolving these sources and processes can aid interpretation of apparent Ar-ages, and the physico-chemical evolution of rhyolitic lava.

The initial argon component of a melt (which may be magmatic, or atmospheric and incorporated during fragmentation and rehealing on eruption) may be modified by heterogeneous degassing and volatile enrichment throughout the lava, both above and below the glass transition, with isotope fractionation occurring during partial degassing. This heterogeneous distribution of Ar-isotopes is retained once the glass cools below the argon closure temperature (measurable Ar-loss would take years at temperatures below ~500 °C). Atmospheric argon is subsequently introduced to parts of the obsidian during hydration, which may happen during and immediately after the eruption, or over

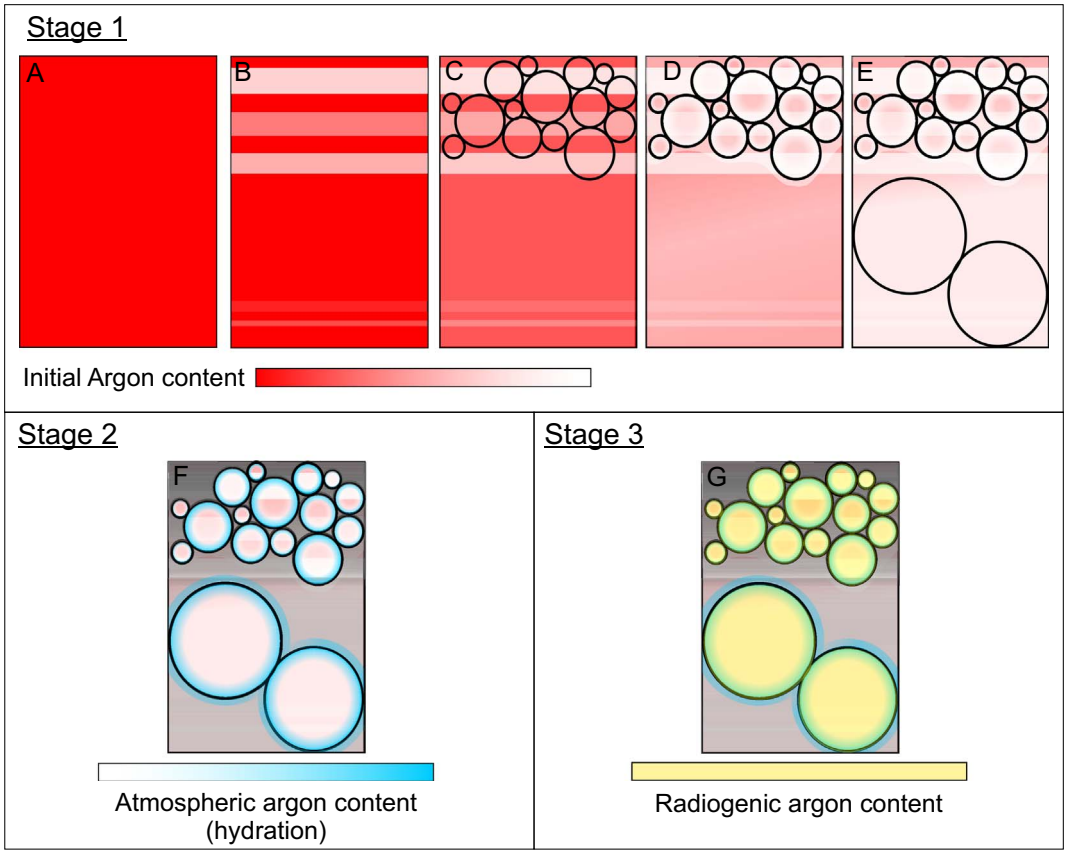

Fig. 12. Summary of argon-isotope evolution in Fragment H. See text for description. Grey areas on Stages 2 and 3 represent devitrified zones, not included in our model. Please refer to the online version of the article for a full colour image.

the millions of years following eruption until the lava has completely devitrified and no glass remains. Deconvolving these two sources of non-radiogenic argon from $^{40}Ar^*$ is essential for reliable K-Ar and $^{40}Ar/^{39}Ar$ dating, but is difficult. The resulting obsidian sample contains a mixture of variably modified argon reservoirs, making isotope correlation diagrams difficult to interpret in terms of eruption age. Initial argon may fractionate during diffusive degassing, with preferential loss of ^{36}Ar, resulting in an apparent excess of ^{40}Ar at diffusion domain rims. These rims of excess ^{40}Ar may be subsequently overprinted by atmospheric Ar during obsidian hydration, making identification of the excess ^{40}Ar impossible to quantitatively identify.

The observed age gradients in the small perlite beads are consistent with degassing profiles of around 500 μm in length (Fig. 6). This length scale is consistent with likely widths of diffusion zones at realistic obsidian cooling rates (Fig. 2).

This study has found no evidence for excess ^{36}Ar, as proposed in other Ar-isotope studies on obsidian (Brown et al., 2009; Morgan et al., 2009), although it is possible that more detailed work on perlite bead rims may reveal a preferential gain of atmospheric ^{36}Ar during hydration. Considering argon solubilities and diffusivities in silicate melts and timescales of obsidian formation, previous hypotheses regarding kinetic fractionation during diffusion of atmospheric argon into obsidian lava flows seem unlikely. However, our data supports models in which kinetic fractionation of Ar-isotopes can influence $^{40}Ar/^{39}Ar$ apparent ages. Contamination in the mass spectrometer at mass 36 has yet to be ruled out, but if this phenomenon is real, a more likely explanation is that atmospheric argon becomes incorporated into the obsidian melt during fragmentation in the vent (Castro et al., 2014; Tuffen et al., 2003), possibly due to a combination of diffusion and surface adsorption, both processes having the potential to induce mass fractionation (van Zuilen et al., 2016).

Our study used one of the oldest obsidian samples available, in the hope that the age would result in high enough $^{40}Ar^*$ yields to provide precise dates from the very small volumes sampled during UV-LAMP analysis. A complimentary experiment will be to analyse zero-age obsidian, to characterise the distribution and isotopic composition of initial argon, without overprinting by $^{40}Ar^*$. Two Chilean volcanoes have erupted rhyolitic obsidian in the last 10 years (Chaitén and Cordén Caulle) and characterisation of Ar-isotope distribution in samples from these eruptions is a logical next step towards testing the hypotheses presented in this study.

When considered in terms of pre-eruption melt storage, subsurface melt degassing may promote preferential loss of ^{36}Ar and thus a melt enriched in excess ^{40}Ar. This may explain how obsidians can contain excess ^{40}Ar, despite being stored and erupted through young, low-K crust (e.g. at Kerlingarfjöll - Flude et al., 2010). More detailed studies on the trapped Ar content of phenocrysts and volcanic glass may thus provide a useful tool to study magma storage and eruption processes.

Acknowledgements

This research was supported by NERC Grant No. NE/E018629/1. Hugh Tuffen is supported by a Royal Society University Research Fellowship. Pete Lipman kindly provided the obsidian sample. James Schwanethal is thanked for general assistance in the Ar-lab. Don Dingwell and Thommy Müller are thanked for inspiring discussions regarding melts, glasses and diffusion.

Appendix A. Supplementary data

Supplementary data to this article can be found online at http://dx.doi.org/10.1016/j.chemgeo.2017.05.018.

References

Amalberti, J., Burnard, P., Laporte, D., Tissandier, L., Neuville, D.R., 2016. Multidiffusion mechanisms for noble gases (He, Ne, Ar) in silicate glasses and melts in the transition temperature domain: implications for glass polymerization. Geochim. Cosmochim. Acta 172, 107–126. http://dx.doi.org/10.1016/j.gca.2015.09.027.

von Aulock, F.W., Nichols, A.R.L., Kennedy, B.M., Oze, C., 2013. Timescales of texture development in a cooling lava dome. Geochim. Cosmochim. Acta 114, 72–80. http://dx.doi.org/10.1016/j.gca.2013.03.012.

von Aulock, F.W., Kennedy, B.M., Schipper, C.I., Castro, J.M., Martin, D.E., Oze, C., Watkins, J.M., Wallace, P.J., Puskar, L., Bégué, F., Nichols, A.R.L., Tuffen, H., 2014. Advances in Fourier transform infrared spectroscopy of natural glasses: from sample preparation to data analysis. Lithos 206–207, 52–64. http://dx.doi.org/10.1016/j.lithos.2014.07.017.

Ballentine, C.J., Barfod, D.N., 2000. The origin of air-like noble gases in MORB and OIB. Earth Planet. Sci. Lett. 180, 39–48. http://dx.doi.org/10.1016/S0012-821X(00)00161-8.

Befus, K.S., 2016. Crystallization kinetics of rhyolitic melts using oxygen isotope ratios: Crystallization kinetics using $\delta^{18}O$. Geophys. Res. Lett. 43, 592–599. http://dx.doi.org/10.1002/2015GL067288.

Behrens, H., 2010a. Ar, CO_2 and H_2O diffusion in silica glasses at 2 kbar pressure. Chem. Geol. 272, 40–48. http://dx.doi.org/10.1016/j.chemgeo.2010.02.001.

Behrens, H., 2010b. Noble gas diffusion in silicate glasses and melts. Rev. Mineral. Geochem. 72, 227–267. http://dx.doi.org/10.2138/rmg.2010.72.6.

Bindeman, I.N., Lowenstern, J.B., 2016. Low-δD hydration rinds in Yellowstone perlites record rapid syneruptive hydration during glacial and interglacial conditions. Contrib. Mineral. Petrol. 171. http://dx.doi.org/10.1007/s00410-016-1293-1.

Brown, F.H., Reid, C., Negash, A., 2009. Possible isotopic fractionation of argon in source obsidians and archeological artifacts from Kulkuletti, Ethiopia. J. Archaeol. Sci. 36, 2119–2124. http://dx.doi.org/10.1016/j.jas.2009.05.008.

Carroll, M.R., 1991. Diffusion of Ar in rhyolite, orthoclase and albite composition glasses. Earth Planet. Sci. Lett. 103, 156–168. http://dx.doi.org/10.1016/0012-821X(91)90157-D.

Carroll, M., Stolper, E., 1991. Argon solubility and diffusion in silica glass: Implications for the solution behavior of molecular gases. Geochim. Cosmochim. Acta 55, 211–225. http://dx.doi.org/10.1016/0016-7037(91)90412-X.

Carroll, M.R., Stolper, E.M., 1993. Noble gas solubilities in silicate melts and glasses: New experimental results for argon and the relationship between solubility and ionic porosity. Geochim. Cosmochim. Acta 57, 5039–5051. http://dx.doi.org/10.1016/0016-7037(93)90606-W.

Castro, J.M., Manga, M., Martin, M.C., 2005. Vesiculation rates of obsidian domes inferred from H_2O concentration profiles. Geophys. Res. Lett. 32. http://dx.doi.org/10.1029/2005GL024029.

Castro, J.M., Beck, P., Tuffen, H., Nichols, A.R.L., Dingwell, D.B., Martin, M.C., 2008. Timescales of spherulite crystallization in obsidian inferred from water concentration profiles. Am. Mineral. 93, 1816–1822. http://dx.doi.org/10.2138/am.2008.2904.

Castro, J.M., Cordonnier, B., Tuffen, H., Tobin, M.J., Puskar, L., Martin, M.C., Bechtel, H.A., 2012. The role of melt-fracture degassing in defusing explosive rhyolite eruptions at volcán Chaitén. Earth Planet. Sci. Lett. 333–334, 63–69. http://dx.doi.org/10.1016/j.epsl.2012.04.024.

Castro, J.M., Bindeman, I.N., Tuffen, H., Ian Schipper, C., 2014. Explosive origin of silicic lava: Textural and δD–H_2O evidence for pyroclastic degassing during rhyolite effusion. Earth Planet. Sci. Lett. 405, 52–61. http://dx.doi.org/10.1016/j.epsl.2014.08.012.

Cerling, T.E., Brown, F.H., Bowman, J.R., 1985. Low-temperature alteration of volcanic glass: Hydration, Na, K, ^{18}O and Ar mobility. Chem. Geol. Isot. Geosci. 52, 281–293. http://dx.doi.org/10.1016/0168-9622(85)90040-5.

Clausen, H.B., Hammer, C.U., Hvidberg, C.S., Dahl-Jensen, D., Steffensen, J.P., Kipfstuhl, J., Legrand, M., 1997. A comparison of the volcanic records over the past 4000 years from the Greenland Ice Core Project and Dye 3 Greenland ice cores. J. Geophys. Res. Oceans 102, 26707–26723. http://dx.doi.org/10.1029/97JC00587.

Denton, J.S., Tuffen, H., Gilbert, J.S., Odling, N., 2009. The hydration and alteration of perlite and rhyolite. J. Geol. Soc. 166, 895–904. http://dx.doi.org/10.1144/0016-76492008-007.

Denton, J.S., Tuffen, H., Gilbert, J.S., 2012. Variations in hydration within perlitised rhyolitic lavas—evidence from Torfajökull, Iceland. J. Volcanol. Geotherm. Res. 223–224, 64–73. http://dx.doi.org/10.1016/j.jvolgeores.2012.02.005.

Fink, J.H., 1983. Structure and emplacement of a rhyolitic obsidian flow: Little Glass Mountain, Medicine Lake Highland, northern California. Geol. Soc. Am. Bull. 94, 362. http://dx.doi.org/10.1130/0016-7606(1983)94<362:SAEOAR>2.0.CO;2.

Flude, S., Storey, M., 2016. $^{40}Ar/^{39}Ar$ age of the Rotoiti Breccia and Rotoehu Ash, Okataina Volcanic Complex, New Zealand, and identification of heterogeneously distributed excess ^{40}Ar in supercooled crystals. Quat. Geochronol. 33, 13–23. http://dx.doi.org/10.1016/j.quageo.2016.01.002.

Flude, S., Burgess, R., McGarvie, D.W., 2008. Silicic volcanism at Ljósufjöll, Iceland: Insights into evolution and eruptive history from Ar–Ar dating. J. Volcanol. Geotherm. Res. 169, 154–175. http://dx.doi.org/10.1016/j.jvolgeores.2007.08.019.

Flude, S., McGarvie, D.W., Burgess, R., Tindle, A.G., 2010. Rhyolites at Kerlingarfjöll, Iceland: the evolution and lifespan of silicic central volcanoes. Bull. Volcanol. 72, 523–538. http://dx.doi.org/10.1007/s00445-010-0344-0.

Friedman, I., Smith, R.L., 1958. The deuterium content of water in some volcanic glasses. Geochim. Cosmochim. Acta 15, 218–228. http://dx.doi.org/10.1016/0016-7037(58)90059-0.

Friedman, I., Smith, R.L., Long, W.D., 1966. Hydration of natural glass and formation of perlite. Geol. Soc. Am. Bull. 77, 323–328. http://dx.doi.org/10.1130/0016-7606(1966)77[323:HONGAF]2.0.CO;2.

Gao, C., Robock, A., Ammann, C., 2008. Volcanic forcing of climate over the past 1500 years: An improved ice core-based index for climate models. J. Geophys. Res. 113. http://dx.doi.org/10.1029/2008JD010239.

Gardner, J.E., Befus, K.S., Watkins, J., Hesse, M., Miller, N., 2012. Compositional gradients surrounding spherulites in obsidian and their relationship to spherulite growth and lava cooling. Bull. Volcanol. 74, 1865–1879. http://dx.doi.org/10.1007/s00445-012-0642-9.

Gilfillan, S.M.V., Ballentine, C.J., Holland, G., Blagburn, D., Lollar, B.S., Stevens, S., Schoell, M., Cassidy, M., 2008. The noble gas geochemistry of natural CO_2 gas reservoirs from the Colorado Plateau and Rocky Mountain provinces, USA. Geochim. Cosmochim. Acta 72, 1174–1198. http://dx.doi.org/10.1016/j.gca.2007.10.009.

Goel, G., Zhang, L., Lacks, D.J., Van Orman, J.A., 2012. Isotope fractionation by diffusion in silicate melts: insights from molecular dynamics simulations. Geochim. Cosmochim. Acta 93, 205–213. http://dx.doi.org/10.1016/j.gca.2012.07.008.

Gottsmann, J., Dingwell, D.B., 2001. The cooling of frontal flow ramps: a calorimetric study on the Rocche Rosse rhyolite flow, Lipari, Aeolian Islands, Italy. Terra Nova 13, 157–164. http://dx.doi.org/10.1046/j.1365-3121.2001.00332.x.

Gottsmann, J., Dingwell, D., 2002. The thermal history of a spatter-fed lava flow: the 8-ka pantellerite flow of Mayor Island, New Zealand. Bull. Volcanol. 64, 410–422. http://dx.doi.org/10.1007/s00445-002-0220-7.

Guillou, H., Van Vliet-Lanoë, B., Guðmundsson, A., Nomade, S., 2010. New unspiked K–Ar ages of Quaternary sub-glacial and sub-aerial volcanic activity in Iceland. Quat. Geochronol. 5, 10–19. http://dx.doi.org/10.1016/j.quageo.2009.08.007.

Helgason, J., Duncan, R.A., 2013. Stratigraphy, Ar-40-Ar-39 dating and erosional history of Svinafell, SE-Iceland. Jökull 63, 33–54.

Huybers, P., Langmuir, C., 2009. Feedback between deglaciation, volcanism, and atmospheric CO_2. Earth Planet. Sci. Lett. 286, 479–491. http://dx.doi.org/10.1016/j.epsl.2009.07.014.

Jezek, P.A., Noble, D.C., 1978. Natural hydration and ion exchange of obsidian: an electron microprobe study. Am. Mineral. 63, 266–273.

Jónasson, K., 1994. Rhyolite volcanism in the Krafla central volcano, north-east Iceland. Bull. Volcanol. 56, 516–528. http://dx.doi.org/10.1007/BF00302832.

Kaneoka, I., 1969. The use of obsidian for K-Ar dating. J. Mass Spectrom. 17, 514–521.

Kaneoka, I., 1972. The effect of hydration on the K/Ar ages of volcanic rocks. Earth Planet. Sci. Lett. 14, 216–220. http://dx.doi.org/10.1016/0012-821X(72)90009-X.

Kelley, S., 2002. Excess argon in K–Ar and Ar–Ar geochronology. Chem. Geol. 188, 1–22. http://dx.doi.org/10.1016/S0009-2541(02)00064-5.

Kuiper, Y.D., 2002. The interpretation of inverse isochron diagrams in $^{40}Ar/^{39}Ar$ geochronology. Earth Planet. Sci. Lett. 203, 499–506. http://dx.doi.org/10.1016/S0012-821X(02)00833-6.

Lachowycz, S.M., Pyle, D.M., Gilbert, J.S., Mather, T.A., Mee, K., Naranjo, J.A., Hobbs, L.K., 2015. Glaciovolcanism at Volcán Sollipulli, southern Chile: lithofacies analysis and interpretation. J. Volcanol. Geotherm. Res. 303, 59–78. http://dx.doi.org/10.1016/j.jvolgeores.2015.06.021.

Lee, J.-Y., Marti, K., Severinghaus, J.P., Kawamura, K., Yoo, H.-S., Lee, J.B., Kim, J.S., 2006. A redetermination of the isotopic abundances of atmospheric Ar. Geochim. Cosmochim. Acta 70, 4507–4512. http://dx.doi.org/10.1016/j.gca.2006.06.1563.

Lipman, P.W., McIntosh, W.C., 2008. Eruptive and noneruptive calderas, northeastern San Juan Mountains, Colorado: where did the ignimbrites come from? Geol. Soc. Am. Bull. 120, 771–795. http://dx.doi.org/10.1130/B26330.1.

Lofgren, G., 1971. Experimentally produced devitrification textures in natural rhyolitic glass. Geol. Soc. Am. Bull. 82, 111. http://dx.doi.org/10.1130/0016-7606(1971)82[111:EPDTIN]2.0.CO;2.

Manley, C.R., Fink, J.H., 1987. Internal textures of rhyolite flows as revealed by research drilling. Geology 15, 549. http://dx.doi.org/10.1130/0091-7613(1987)15<549:ITORFA>2.0.CO;2.

Mark, D.F., Petraglia, M., Smith, V.C., Morgan, L.E., Barfod, D.N., Ellis, B.S., Pearce, N.J., Pal, J.N., Korisettar, R., 2014. A high-precision $^{40}Ar/^{39}Ar$ age for the Young Toba Tuff and dating of ultra-distal tephra: forcing of Quaternary climate and implications for hominin occupation of India. Quat. Geochronol. 21, 90–103. http://dx.doi.org/10.1016/j.quageo.2012.12.004.

McDougall, I., Harrison, T.M., 1999. Geochronology and Thermochronology by the $^{40}Ar/^{39}Ar$ Method, second ed. Oxford University Press.

McGarvie, D.W., 1984. Torfajökull: a volcano dominated by magma mixing. Geology 12, 685–688. http://dx.doi.org/10.1130/0091-7613(1984)12<685:TAVDBM>2.0.CO;2.

McGarvie, D., 2009. Rhyolitic volcano-ice interactions in Iceland. J. Volcanol. Geotherm. Res. 185, 367–389. http://dx.doi.org/10.1016/j.jvolgeores.2008.11.019.

McGarvie, D.W., Burgess, R., Tindle, A.G., Tuffen, H., Stevenson, J.A., 2006. Pleistocene rhyolitic volcanism at the Torkfajökull central volcano, Iceland: eruption ages, ice-volcano interactions, and geochemical evolution. Jökull 56, 57–75.

McGarvie, D.W., Stevenson, J.A., Burgess, R., Tuffen, H., Tindle, A.G., 2007. Volcano–ice interactions at Prestahnúkur, Iceland: rhyolite eruption during the last interglacial–glacial transition. Ann. Glaciol. 45, 38–47. http://dx.doi.org/10.3189/172756407782282453.

Mee, K., Tuffen, H., Gilbert, J.S., 2006. Snow-contact volcanic facies and their use in determining past eruptive environments at Nevados de Chillán volcano, Chile. Bull. Volcanol. 68, 363–376. http://dx.doi.org/10.1007/s00445-005-0017-6.

Mee, K., Gilbert, J.S., McGarvie, D.W., Naranjo, J.A., Pringle, M.S., 2009. Palaeoenvironment reconstruction, volcanic evolution and geochronology of the Cerro Blanco subcomplex, Nevados de Chillán volcanic complex, central Chile. Bull. Volcanol. 71, 933–952. http://dx.doi.org/10.1007/s00445-009-0277-7.

Morgan, L.E., Renne, P.R., Taylor, R.E., WoldeGabriel, G., 2009. Archaeological age constraints from extrusion ages of obsidian: examples from the Middle Awash, Ethiopia. Quat. Geochronol. 4, 193–203. http://dx.doi.org/10.1016/j.quageo.2009.

01.001.
Newman, S., Stolper, E.M., Epstein, S., 1986. Measurement of water in rhyolitic glasses; calibration of an infrared spectroscopic technique. Am. Mus. Novit. 71, 1527–1541.
Owen, J., Tuffen, H., McGarvie, D., 2012. Using dissolved H_2O in rhyolitic glasses to estimate palaeo-ice thickness during a subglacial eruption at Bláhnúkur (Torfajökull, Iceland). Bull. Volcanol. 74, 1355–1378. http://dx.doi.org/10.1007/s00445-012-0601-5.
Ozima, M., Podosek, F.A., 2002. Noble Gas Geochemistry, second ed. Cambridge University Press.
Paonita, A., Caracausi, A., Iacono-Marziano, G., Martelli, M., Rizzo, A., 2012. Geochemical evidence for mixing between fluids exsolved at different depths in the magmatic system of Mt Etna (Italy). Geochim. Cosmochim. Acta 84, 380–394. http://dx.doi.org/10.1016/j.gca.2012.01.028.
Rampino, M.R., Self, S., 1992. Volcanic winter and accelerated glaciation following the Toba super-eruption. Nature 359, 50–52. http://dx.doi.org/10.1038/359050a0.
Renne, P.R., Swisher, C.C., Deino, A.L., Karner, D.B., Owens, T.L., DePaolo, D.J., 1998. Intercalibration of standards, absolute ages and uncertainties in $^{40}Ar/^{39}Ar$ dating. Chem. Geol. 145, 117–152. http://dx.doi.org/10.1016/S0009-2541(97)00159-9.
Richter, F.M., Davis, A.M., DePaolo, D.J., Watson, E.B., 2003. Isotope fractionation by chemical diffusion between molten basalt and rhyolite. Geochim. Cosmochim. Acta 67, 3905–3923. http://dx.doi.org/10.1016/S0016-7037(03)00174-1.
Richter, F.M., Watson, E.B., Mendybaev, R.A., Teng, F.-Z., Janney, P.E., 2008. Magnesium isotope fractionation in silicate melts by chemical and thermal diffusion. Geochim. Cosmochim. Acta 72, 206–220. http://dx.doi.org/10.1016/j.gca.2007.10.016.
Richter, F., Dauphas, N., Teng, F., 2009. Non-traditional fractionation of non-traditional isotopes: evaporation, chemical diffusion and Soret diffusion. Chem. Geol. 258, 92–103. http://dx.doi.org/10.1016/j.chemgeo.2008.06.011.
Ross, C.S., Smith, R.L., 1955. Water and other volatiles in volcanic glasses. Am. Mineral. 40, 1071–1089.
Ryan, A.G., Russell, J.K., Nichols, A.R.L., Hess, K.-U., Porritt, L.A., 2015. Experiments and models on H_2O retrograde solubility in volcanic systems. Am. Mineral. 100, 774–786. http://dx.doi.org/10.2138/am-2015-5030.
Saubin, E., Tuffen, H., Gurioli, L., Owen, J., Castro, J.M., Berlo, K., McGowan, E.M., Schipper, C.I., Wehbe, K., 2016. Conduit Dynamics in Transitional Rhyolitic Activity Recorded by Tuffisite Vein Textures from the 2008–2009 Chaitén Eruption. Front. Earth Sci. 4. http://dx.doi.org/10.3389/feart.2016.00059.
Seaman, S.J., 2013. Microtexture development during rapid cooling in three rhyolitic lava flows. Am. Mineral. 98, 304–318. http://dx.doi.org/10.2138/am.2013.4313.
Sherlock, S.C., Arnaud, N.O., 1999. Flat plateau and impossible isochrons: apparent ^{40}Ar-^{39}Ar geochronology in a high-pressure terrain. Geochim. Cosmochim. Acta 63, 2835–2838. http://dx.doi.org/10.1016/S0016-7037(99)00116-7.
Sigl, M., Winstrup, M., McConnell, J.R., Welten, K.C., Plunkett, G., Ludlow, F., Büntgen, U., Caffee, M., Chellman, N., Dahl-Jensen, D., Fischer, H., Kipfstuhl, S., Kostick, C., Maselli, O.J., Mekhaldi, F., Mulvaney, R., Muscheler, R., Pasteris, D.R., Pilcher, J.R., Salzer, M., Schüpbach, S., Steffensen, J.P., Vinther, B.M., Woodruff, T.E., 2015. Timing and climate forcing of volcanic eruptions for the past 2,500 years. Nature 523, 543–549. http://dx.doi.org/10.1038/nature14565.
Smellie, J.L., Rocchi, S., Armienti, P., 2011a. Late Miocene volcanic sequences in northern Victoria Land, Antarctica: products of glaciovolcanic eruptions under different thermal regimes. Bull. Volcanol. 73, 1–25. http://dx.doi.org/10.1007/s00445-010-0399-y.
Smellie, J.L., Rocchi, S., Gemelli, M., Di Vincenzo, G., Armienti, P., 2011b. A thin predominantly cold-based Late Miocene East Antarctic ice sheet inferred from glaciovolcanic sequences in northern Victoria Land, Antarctica. Palaeogeogr. Palaeoclimatol. Palaeoecol. 307, 129–149. http://dx.doi.org/10.1016/j.palaeo.2011.05.008.
Smellie, J.L., Rocchi, S., Wilch, T.I., Gemelli, M., Di Vincenzo, G., McIntosh, W., Dunbar, N., Panter, K., Fargo, A., 2014. Glaciovolcanic evidence for a polythermal Neogene East Antarctic Ice Sheet. Geology 42, 39–41. http://dx.doi.org/10.1130/G34787.1.
Spell, T., McDougall, I., 2003. Characterization and calibration of $^{40}Ar/^{39}Ar$ dating standards. Chem. Geol. 198, 189–211. http://dx.doi.org/10.1016/S0009-2541(03)00005-6.
Stasiuk, M.V., Barclay, J., Carroll, M.R., Jaupart, C., Ratté, J.C., Sparks, R.S.J., Tait, S.R., 1996. Degassing during magma ascent in the Mule Creek vent (USA). Bull. Volcanol. 58, 117–130. http://dx.doi.org/10.1007/s004450050130.
Steiger, R.H., Jäger, E., 1977. Subcommission on geochronology: convention on the use of decay constants in geo- and cosmochronology. Earth Planet. Sci. Lett. 36, 359–362. http://dx.doi.org/10.1016/0012-821X(77)90060-7.
Stevenson, J.A., McGarvie, D.W., Smellie, J.L., Gilbert, J.S., 2006. Subglacial and ice-contact volcanism at the Öræfajökull stratovolcano, Iceland. Bull. Volcanol. 68, 737–752. http://dx.doi.org/10.1007/s00445-005-0047-0.
Stevenson, J.A., Smellie, J.L., McGarvie, D.W., Gilbert, J.S., Cameron, B.I., 2009. Subglacial intermediate volcanism at Kerlingarfjöll, Iceland: Magma–water interactions beneath thick ice. J. Volcanol. Geotherm. Res. 185, 337–351. http://dx.doi.org/10.1016/j.jvolgeores.2008.12.016.
Storey, M., Roberts, R.G., Saidin, M., 2012. Astronomically calibrated $^{40}Ar/^{39}Ar$ age for the Toba supereruption and global synchronization of late Quaternary records. Proc. Natl. Acad. Sci. http://dx.doi.org/10.1073/pnas.1208178109.
Tuffen, H., Dingwell, D.B., Pinkerton, H., 2003. Repeated fracture and healing of silicic magma generate flow banding and earthquakes? Geology 31, 1089. http://dx.doi.org/10.1130/G19777.1.
Tuffen, H., Owen, J., Denton, J., 2010. Magma degassing during subglacial eruptions and its use to reconstruct palaeo-ice thicknesses. Earth Sci. Rev. 99, 1–18. http://dx.doi.org/10.1016/j.earscirev.2010.01.001.
Vogel, N., Nomade, S., Negash, A., Renne, P.R., 2006. Forensic $^{40}Ar/^{39}Ar$ dating: a provenance study of Middle Stone Age obsidian artifacts from Ethiopia. J. Archaeol. Sci. 33, 1749–1765. http://dx.doi.org/10.1016/j.jas.2006.03.008.
Watkins, J., Manga, M., Huber, C., Martin, M., 2008. Diffusion-controlled spherulite growth in obsidian inferred from H_2O concentration profiles. Contrib. Mineral. Petrol. 157, 163–172. http://dx.doi.org/10.1007/s00410-008-0327-8.
Wilding, M.C., Webb, S.L., Dingwell, D.B., 1995. Evaluation of a relaxation geospeedometer for volcanic glasses. Chem. Geol. 125, 137–148. http://dx.doi.org/10.1016/0009-2541(95)00067-V.
van Zuilen, K., Müller, T., Nägler, T.F., Dietzel, M., Küsters, T., 2016. Experimental determination of barium isotope fractionation during diffusion and adsorption processes at low temperatures. Geochim. Cosmochim. Acta 186, 226–241. http://dx.doi.org/10.1016/j.gca.2016.04.049.